Titre: Title:	Experimental Evaluation of the Performance of Event-Based Cameras for Particle Image Velocimetry
Auteur: Author:	Luisa Fernanda Maya Murcia
Date:	2025
Type:	Mémoire ou thèse / Dissertation or Thesis
Référence: Citation:	Maya Murcia, L. F. (2025). Experimental Evaluation of the Performance of Event-Based Cameras for Particle Image Velocimetry [Master's thesis, Polytechnique Montréal]. PolyPublie. https://publications.polymtl.ca/68782/

POLYTECHNIQUE MONTRÉAL
affiliée à l'Université de Montréal

Experimental Evaluation of the Performance of Event-Based Cameras for Particle Image Velocimetry

LUISA FERNANDA MAYA MURCIA
Département de génie mécanique

Mémoire présenté en vue de l'obtention du diplôme de *Maîtrise ès sciences appliquées*
Génie mécanique

Août 2025

POLYTECHNIQUE MONTRÉAL
affiliée à l'Université de Montréal

Ce mémoire intitulé :

Experimental Evaluation of the Performance of Event-Based Cameras for Particle Image Velocimetry

présenté par **Luisa Fernanda MAYA MURCIA**
en vue de l'obtention du diplôme de *Maîtrise ès sciences appliquées*
a été dûment accepté par le jury d'examen constitué de :

Bianca VIGGIANO, présidente
Bruno SAVARD, membre et directeur de recherche
Patrizio VENA, membre et codirecteur de recherche
Jérôme VÉTEL, membre

DEDICATION

To my family and to Felipe,
who believed in me every step of the way.

ACKNOWLEDGEMENTS

I would like to express my deepest gratitude to my research supervisors, Bruno Savard and Patrizio Vena, for their unwavering support, mentorship, and trust throughout this journey. Their curiosity and enthusiasm encouraged me to venture into research areas I had never imagined myself exploring. Thank you for showing me how to navigate situations I never thought I could face, for supporting me through difficult moments, and for reminding me that before being researchers or engineers, we are human beings. I am grateful for the privilege of learning from your brilliant minds and exciting ideas, and for welcoming me into scientific environments like Polytechnique Montréal and National Research Council (NRC) Ottawa, places full of knowledge, extraordinary thinkers, and, most importantly, remarkable people.

To my mentor, Luming Fan, thank you for your time, your patience, and your deep knowledge. Thank you for sitting beside me on so many afternoons, helping me through times when I felt lost, and for always being open to sharing everything you know about subjects that were entirely new to me. You guided me step by step throughout my master's, and your passion for teaching and scientific rigor have left a mark on me. Thank you also for valuing my work in ways I hadn't perceived myself, and for elevating it to an academic level I never imagined.

To Philippe Versailles, research associate at Polytechnique Montréal, thank you for guiding me through the execution of my first experiments, for your generous help over many days, and for being such a reliable teammate. Your ideas, support, and expertise in experimental work helped me solve challenges and made me feel confident throughout the process. And to Antoine Durocher, research officer at NRC, thank you for teaching me the practical aspects of lab work, for being consistently involved in my progress, and for always offering valuable and insightful suggestions.

To my family, thank you for believing in me at every step, for supporting me with love, and for always trusting that I can achieve anything I set my mind to.

And to my husband, Felipe, you are my anchor. You've stood by me in hard times, worked shoulder-to-shoulder with me, and in moments of frustration, you've sat beside me, studied with me, tried to understand, and helped me through challenges I thought were beyond me. You've always believed in me, even more than I believe in myself. And you're right, I am strong, but I'm stronger with you by my side.

Finally, I want to thank myself, for my persistence and for daring to dream big.

This research was supported by funding from the NRC's Aerospace Strategic Client Services

program, the Natural Sciences and Engineering Research Council of Canada (RGPIN-2019-04309, RGPAS-2019-00131), and Environment and Climate Change Canada.

RÉSUMÉ

Les caméras événementielles sont un nouveau type de capteur de vision qui enregistrent de manière asynchrone les changements de luminosité avec une précision de l'ordre de la microseconde. Elles offrent plusieurs avantages par rapport aux systèmes traditionnels basés sur des images, notamment une plage dynamique élevée, une faible consommation d'énergie et la capacité de capturer des mouvements rapides sans flou de mouvement. Cependant, malgré ces avantages, les caméras événementielles présentent également des limites lorsqu'elles sont utilisées pour le diagnostic des écoulements fluides, notamment une résolution spatiale inférieure, une latence de lecture et des contraintes de bande passante limitées par rapport aux caméras à haute vitesse. Cette thèse vise à évaluer les performances en termes de latence et de bande passante des caméras événementielles pour la vélocimétrie par images de particules (PIV) et à identifier les conditions expérimentales dans lesquelles leurs caractéristiques uniques peuvent être exploitées efficacement.

Une série d'expériences a été réalisée avec une illumination laser pulsée, répartie en deux groupes principaux. La première série visait à caractériser les performances de la caméra en éclairant une cuvette d'eau contenant des particules traceuses à l'aide d'impulsions laser uniques. Cette configuration nous a permis d'étudier la réponse du capteur en termes de latence et de bande passante à différents taux d'événements. Nous avons caractérisé ces limites en analysant la distribution temporelle de la génération d'événements et en reconstruisant des pseudo-images. À partir de cette analyse, nous avons identifié la limite de bande passante de la caméra avant que la saturation de lecture ne se produise, soit environ 400 événements/µs, et avons établi une relation claire entre le taux d'événements et la latence. Ces résultats nous ont permis de définir les conditions optimales pour les applications PIV. Nous avons également examiné comment la densité d'ensemencement et l'éclairage affectent la génération d'événements, révélant ainsi les régimes opérationnels pour lesquels des mesures de vitesse précises peuvent être obtenues. D'autres paramètres, tels que la taille de l'image des particules et le seuil de contraste, ont été évalués afin de mieux comprendre leur impact sur les performances.

La deuxième série d'expériences consistait en des mesures PIV avec un éclairage à double impulsion dans des jets d'air. Les résultats étaient conformes aux directives établies lors des tests de caractérisation et ont été validés à l'aide d'une caméra sCMOS comme référence. Les résultats démontrent que les capteurs événementiels peuvent reconstruire de manière fiable des champs de vitesse allant jusqu'à 1.8 m/s (0.03 px/µs). Les densités d'images de

particules supérieures à 0.018 ppp ont donné des valeurs d'incertitude inférieures à 0.4 px dans nos conditions spécifiques, ce qui confirme le potentiel des caméras événementielles comme alternative compacte et économe en énergie aux caméras à grande vitesse dans les conditions définies.

Ce mémoire établit les limites d'applicabilité des caméras événementielles pour la PIV dans nos conditions expérimentales spécifiques, tout en reconnaissant que ces limites peuvent varier en fonction de la région d'intérêt, des paramètres de la caméra ou des modèles de matériel, en particulier à mesure que la technologie continue d'évoluer. En identifiant les seuils de performance clés pour des mesures de vitesse précises et en analysant comment la génération d'événements est influencée par les paramètres discutés ci-dessus, ce travail contribue à l'effort continu visant à adapter l'imagerie événementielle au diagnostic des fluides. Au-delà des résultats eux-mêmes, la méthodologie expérimentale développée ici fournit un cadre pratique pour évaluer les performances des caméras événementielles dans de nouvelles configurations ou avec du matériel différent, facilitant ainsi leur intégration dans des installations expérimentales de mécanique des fluides.

ABSTRACT

Event-based cameras are a novel type of vision sensor that asynchronously record changes in brightness with microsecond precision, offering several advantages over traditional frame-based systems, including high dynamic range, low power consumption, and the ability to capture high-speed motion without motion blur. However, despite these benefits, event cameras also present limitations when applied to fluid flow diagnostics, which includes lower spatial resolution, readout latency, and limited bandwidth constraints compared to high-speed cameras. This thesis aims to evaluate the latency and bandwidth performance of event-based cameras for Particle Image Velocimetry (PIV) and to identify the experimental conditions under which their unique characteristics can be effectively leveraged.

A series of experiments was conducted using pulsed laser illumination, divided into two main groups. The first set focused on characterizing the camera's performance by illuminating a water cuvette seeded with tracer particles using single laser pulses. This setup allowed us to study the sensor's response in terms of latency and bandwidth under varying event rates. We characterized these limitations by analyzing the temporal distribution of event generation and reconstructing pseudo-frames. From this analysis, we identified the bandwidth limit of the camera before readout saturation occurs approximately at 400 events/µs and established a clear relationship between event rate and latency. These findings enabled us to define optimal conditions for PIV applications. We also examined how seeding density and illumination affect event generation, revealing operational regimes for which accurate velocity measurements can be obtained. Additional parameters such as particle image size and contrast threshold were evaluated to further understand their impact on performance.

The second set of experiments consisted of PIV measurements with double-pulse illumination in air jets. The results were consistent with the guidelines established in the characterization tests and were further validated using a sCMOS camera as a reference. The findings demonstrate that event-based sensors can reliably reconstruct velocity fields up to 1.8 m/s (0.03 px/µs). Particle image densities above 0.018 ppp yielded uncertainty values below 0.4 px under our specific conditions, supporting the potential of event cameras as a compact, energy-efficient alternative to high-speed cameras at the defined conditions.

This thesis establishes the applicability limits of event cameras for PIV under our specific experimental conditions, while acknowledging that these boundaries may shift with variations in the region of interest, camera parameters, or hardware models, particularly as the technology continues to evolve. By identifying key performance thresholds for accurate ve-

locity measurements and analyzing how event generation is influenced by the parameters discussed above, this work contributes to the ongoing effort to adapt event-based imaging to fluid diagnostics. Beyond the results themselves, the experimental methodology developed here provides a practical framework for evaluating the performance of event cameras in new configurations or with different hardware, supporting their integration into experimental fluid mechanics setups.

TABLE OF CONTENTS

DEDICATION iii

ACKNOWLEDGEMENTS iv

RÉSUMÉ vi

ABSTRACT viii

LIST OF TABLES xii

LIST OF FIGURES xiii

LIST OF SYMBOLS AND ACRONYMS xvii

CHAPTER 1 INTRODUCTION 1
1.1 Motivation 1
1.2 Fluid Velocimetry 3
1.3 Frame-Based Cameras 5
1.4 Event-Based Cameras 7
1.4.1 Bio-Inspired Design and Principle of Operation 7
1.4.2 Read-out Process 11
1.5 Particle Velocimetry with Event-Based Cameras 13
1.5.1 Planar Event-Based Particle Tracking Velocimetry 16
1.5.2 3D Event-Based Particle Tracking Velocimetry 17
1.5.3 Event-Based Particle Image Velocimetry 18
1.5.4 New Developments in Event-Based Particle Velocimetry 20
1.6 Research Scope 21
1.6.1 Knowledge Gap 21
1.6.2 Research Objectives 22
1.6.3 Structure of the Thesis 23

CHAPTER 2 ARTICLE 1: AN EVALUATION OF EVENT-BASED CAMERAS FOR PARTICLE IMAGE VELOCIMETRY 24
2.1 Introduction 25
2.2 Experimental Methods 28
2.2.1 Test conditions 29
2.3 Event camera characterization test using a water/alumina suspension in a cuvette 31

2.3.1 Response to pulsed laser illumination 31
2.3.2 Latency 33
2.3.3 Information loss 35
2.3.4 Effect of laser pulse energy 38
2.3.5 Particle image density 40
2.3.6 Particle image size 43
2.3.7 Effect of contrast threshold 45
2.4 Event-based PIV measurements in a seeded air jet 46
2.4.1 Velocity dynamic range 47
2.4.2 Uncertainty analysis 51
2.4.3 Column-wise latency and adaptive accumulation time 52
2.5 Conclusion 55

CHAPTER 3 CONCLUSION 58
3.1 Summary of Works 58
3.2 Limitations 59
3.3 Future Research 59

REFERENCES 61

LIST OF TABLES

Table 1.1 Event-Based Particle Velocimetry Summary 13
Table 2.1 Configuration of the optical system 30
Table 2.2 Summary of test conditions 31

LIST OF FIGURES

Figure 1.1 Timeline of event camera development 2

Figure 1.2 Low, medium, and high particle image density for different velocimetry operation modes 3

Figure 1.3 Typical PIV set-up for 2D PIV in a wind tunnel 4

Figure 1.4 Principle of operation of a frame-based camera 6

Figure 1.5 Impact of exposure time on motion blur during high-speed imaging of a target rotating at 25 Hz 7

Figure 1.6 Event camera pixel circuit compared to human retina 8

Figure 1.7 Principle of event generation in an event camera 9

Figure 1.8 Visual comparison between the output of a conventional frame-based camera (top) and an event-based camera (bottom) tracking a fast-moving object 10

Figure 1.9 Chip block diagram illustrating the readout architecture of an event camera 12

Figure 2.1 Experimental setup 29

Figure 2.2 Temporal distribution of ON and OFF events following a 14.4 mJ laser pulse and particle image density of 2×10^{-2} ppp. The bin width is 50 μs 32

Figure 2.3 Temporal distribution of events generated in response to a laser pulse for reference case (red bins), and relative increases in laser energy (green bins) and seeding density (gray bins). The legend indicates the total number of ON events induced by the laser pulse. The instantaneous event rate is calculated based on a 50 μs bin size. Average event rates over the entire event distribution of the three cases are 50 ev/μs, 112.9 ev/μs and 210.5 ev/μs, respectively 34

Figure 2.4 Latency distribution of the EVK2 Gen 4.2 as a function of event rate for data series E and S in the water/alumina suspension 35

Figure 2.5 Reconstructed pseudo-images generated from four different seeding cases in the S data series, accumulated over various time intervals. Only ON events are presented. The laser energy was 14.4 mJ and the particle image densities a) 3.7×10^{-3}, b) 2.0×10^{-2}, c) 4.5×10^{-2}, and d) 1.0×10^{-1} ppp. The corresponding latency values were a) 255 μs, b) 405 μs, c) 461 μs, and d) 358 μs 37

Figure 2.6 (a) Number of active rows at different tested event rates, post-processed using various accumulation times. Each dot represents a pseudo-image reconstructed from a single laser pulse. For each of the 61 tested conditions in data series E and S, 200 laser pulses were recorded and processed. *acc=latency* refers to an accumulation time long enough to capture all the events generated by the corresponding laser pulse, varying for each case; (b) Maximum event rate for each accumulation time that ensures that at least 95% of rows are captured in the pseudo-image reconstruction. The error bars represent the shot-to-shot standard deviation 38

Figure 2.7 sCMOS images (top) and event pseudo-images (bottom) for three different laser energies and the same region of interest (ROI). In (a), red circles indicate the position of particles detected by the event camera, overlaid on the corresponding sCMOS image 40

Figure 2.8 Particle image density (left y-axis) for sCMOS and event camera, and event rate (right y-axis) as a function of laser energy for the E data series. Each point on the graph represents the mean value calculated from 200 images for a fixed seeding density 41

Figure 2.9 Event rate as a function of particle image density for S-series data, collected at 14.4 mJ laser energy 42

Figure 2.10 Event pseudo-images of the water/alumina suspension for three increasing levels of defocus, with equivalent particle image diameters of 1.6, 4.5, and 8.6 pixels, respectively. The fully focused reference pseudo-image in (a) corresponds to a particle image density of 2.2×10^{-3} ppp, compared to 1.8×10^{-4} in (b) and 9×10^{-6} ppp in (c) . . . 44

Figure 2.11 Number of particles and events per particle for various equivalent particle sizes at different defocusing levels. The seeding density and laser energy were held constant at 3.8×10^9 particle/m^3 and 14.4 mJ, respectively 44

Figure 2.12 Number of events per particle for data series E, S, and P for event rates below the maximum of 400 ev/μs, such that non-retrievable information loss is not observed. Triangle markers represent an additional test case with particle aggregates, while square markers correspond to defocused conditions used to intentionally produce larger particle image sizes. The color bar indicates the seeding density in particles/m^3, quantified at a laser energy of 14.4 mJ 45

Figure 2.13 Impact of varying the contrast threshold (C data series) on the number of detected particles and latency in the event camera 46

Figure 2.14 Event distribution following first and second PIV laser pulses, corresponding Mie scattering event pseudo-images, and resulting vector fields for air jets with bulk velocities 0.2, 0.5, 0.8, 1.2, 2, and 5 m/s (Re = 1355, 3387, 5419 for D = 100 mm, and 2560, 4267, 10667 for D = 32 mm, respectively). The pulse intervals were set to 500, 400, 250, 200, 120, and 30 μs, respectively, ensuring that particle displacements in high-velocity regions of the flow remained within 3–7 pixels. For both the event and sCMOS cameras, particle displacements typically fell within one quarter of the interrogation window size. The laser pulse energy was approximately 14.4 mJ 48

Figure 2.15 Six example instantaneous vector fields from the 1.2 m/s air jet, plotted onto Figure 2.6 at a pulse interval of 200 μs. The corresponding event rates and particle image densities are: (a) 30.0 ev/μs - 9.7×10^{-3} ppp, (b) 65.4 ev/μs - 18.5×10^{-3} ppp, (c) 94.4 ev/μs - 2.7×10^{-2} ppp, (d) 123.4 ev/μs - 3.4×10^{-2} ppp, (e) 196.3 ev/μs - 5.0×10^{-2} ppp and (f) 320.2 ev/μs - 6.5×10^{-2} ppp 50

Figure 2.16 Uncertainty of the event camera and RMSE between the event camera and sCMOS camera. In (a) and (b) at 1.2 m/s with the 32 mm converging nozzle, and (c) and (d) at 1 m/s with the 100 mm tube. The shaded gray area in (a) and (b) highlights the region evaluated in (c) and (d) for comparison. Each point in the plot represents a single velocity vector field. The pulse interval was fixed at 200 μs 53

Figure 2.17 Example EBIV pseudo-images in (a) and (b) investigating the feasibility of adaptive event accumulation. Column 1-2: the first and second frames are reconstructed using a global accumulation time (equal to the laser pulse interval 200 μs). Regions a and b indicate missing column bands, while ref marks a reference region with no missing columns. The colormap shows the timestamp at which each column was read out. Column 3: local event distributions (bin size = 10 μs) extracted from each 5-column-wide band (a, b, and ref). Column 4-5: reconstructed first and second frames using adaptive accumulation. The event rate in (a) and (b) was $\sim$ 200 ev/μs, non-retrievable information loss was not observed 54

Figure 2.18 Event-based velocity fields obtained using global and adaptive accumulation times compared to a reference sCMOS camera for test cases (a) and (b) from Figure 2.17 55

LIST OF SYMBOLS AND ACRONYMS

ATIS	Asynchronous Time-based Image Sensor
CAGR	Compound Annual Growth Rate
CCD	Charge-Coupled Device
CW	Continuous Wave
DAVIS	Dynamic and Active-pixel Vision Sensor
DVS	Dynamic Vision Sensor
EBIV	Event-Based Image Velocimetry
ESP	Event Signal Processing
EVK	Evaluation Kit
FIFO	First In First Out
FOV	Field of View
fps	frames per second
HD	High Definition
HDR	High Dynamic Range
kB	kilobyte
LED	Light Emitting Diode
LPT	Lagrangian Particle Tracking
LSV	Laser Speckle Velocimetry
MB	megabyte
MEPS	Millions of Events Per Second
NRC	National Research Council
PEV	Particle Event Velocimetry
PIV	Particle Image Velocimetry
ppp	particles per pixel
PTV	Particle Tracking Velocimetry
PWM	Pulse Width Modulation
Re	Reynolds number
RMSE	Root Mean Square Error
ROI	Region of Interest
sCMOS	scientific Complementary Metal-Oxide-Semiconductor

CHAPTER 1 INTRODUCTION

1.1 Motivation

Reducing greenhouse gas emissions, for example by improving the efficiency of energy systems and advancing clean combustion technologies, is among the biggest challenges our society faces in tackling climate change and promoting sustainable development. Many of the processes at the core of these efforts, such as fuel injection, mixing, and combustion, among others, are governed by complex turbulent flows. In reciprocating engines, gas turbines, and industrial burners, understanding and controlling these turbulent flows is essential to reducing pollutant formation and maximizing efficiency. Accurately measuring velocity fields in such flows is therefore critical for experimental investigations and for validating computational models that aim to optimize systems performance and reduce emissions.

While various techniques exist for measuring fluid flow velocity [1], one of the most common is the use of cameras to detect the displacement of particles carried by the flow over a given time [2,3]. Nowadays, high-speed cameras can be employed for this purpose [4]. However, this technology is expensive, power-consuming, and requires large storage capacities to save the captured data. As a result, its use is often limited to applications involving very high-speed flows or cases where extremely high precision is required.

Event cameras are a new, emerging technology that has the potential to rival traditional high-speed cameras in a variety of applications, including flow velocity measurements. Its inception can be traced back to 1989 when a group of researchers from Caltech introduced the concept of neuromorphic engineering, a field inspired by the architecture of biological neural systems [5–7]. Their goal was to develop hardware and computational models that mimic the way the brain processes information, leading to more efficient and adaptive technologies. In the early 1990s Mahowald and Mead [8] developed a sensor known as “Silicon Retina”. Inspired by the behavior of the human eye, this sensor marked a breakthrough in computer vision. Over time, this technology has evolved into what we now know as event cameras. Through continuous efforts from both academia and industry, event cameras have seen significant improvements in resolution, pixel size, and bandwidth. Figure 1.1 shows a timeline of various event camera models and their feature enhancements over the years. This innovative and disruptive technology offers a more accessible alternative to traditional high-speed cameras. It is energy-efficient, requires significantly less storage capacity for captured data, and is much smaller in size, making it portable and easy to install in tight spaces.

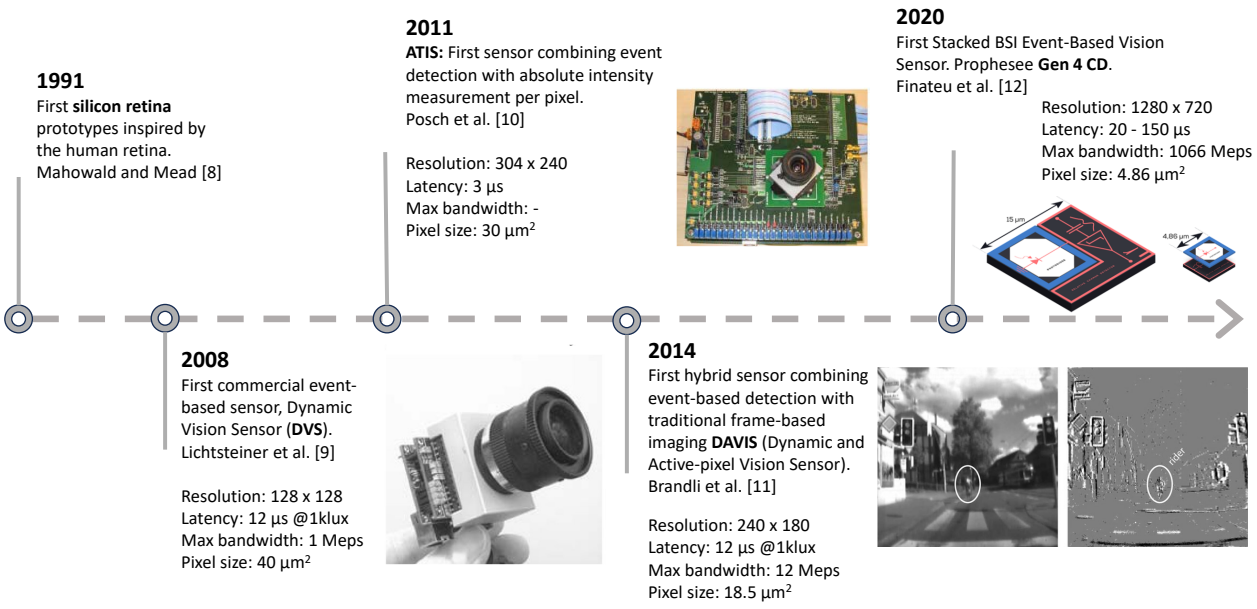

Figure 1.1 Timeline of event camera development ("Meps" denotes millions of events per second). Adapted from [9–12]

However, the use of cameras extends far beyond fluid flow measurement. Today, cameras play a key role in many engineering applications involving motion, such as robotics, monitoring and surveillance, autonomous vehicles, and aerospace navigation. In these scenarios, event cameras have the potential to play a leading role due to their precise temporal resolution. Another significant advantage of event cameras is their ability to handle fast motion with minimal blur and at a lower power consumption. This makes them especially suitable for battery-powered devices, such as drones and industrial automation systems. Furthermore, event cameras are significantly more affordable than traditional high-speed cameras, with costs estimated at approximately one-third for the same spatiotemporal resolution [13]. According to a recent market analysis, the global event camera module market size was valued at approximately $7.06 billion in 2024 and is expected to grow to nearly $20.29 billion by 2032, with a compound annual growth rate (CAGR) of roughly 14.1% [14]. As a growing field, it is essential to evaluate how this technology performs across its various potential applications, where it can contribute as a technological advancement with societal impact, while also identifying areas for improvement.

In this work, we explore the use of event cameras for fluid flow velocity measurements to assess their potential as a more accessible and efficient alternative to traditional high-speed cameras. By characterizing their performance and comparing it to conventional methods, we aim to define the conditions under which they can be applied in this field. This evaluation of-

fers an opportunity to expand the range of tools available for studying flows and turbulence, particularly in scenarios where conventional systems fall short, such as in laser-restricted environments, high dynamic range scenes, or setups constrained by space, or budget. The low power consumption and portability of event cameras also support the development of lightweight, energy-efficient measurement systems, well suited for applications like microfluidic diagnostics and drone-based measurements. Ultimately, this work contributes to the growing adoption of event-based sensing in both research and industrial flow diagnostics.

1.2 Fluid Velocimetry

The measurement of fluid flow velocity is a well established area of research, with various techniques developed to reconstruct velocity vector fields. These techniques typically involve seeding the fluid with fine particles and illuminating them with a laser to track their motion, which reveals the flow patterns, both laminar and turbulent. Depending on the particle image density in the flow, different operating modes are used. From highest to lowest particle concentration, these modes are: laser speckle velocimetry (LSV), high image density particle image velocimetry (PIV), and particle tracking velocimetry (PTV) [15], with the latter two being the most commonly employed. Typical seeding densities for the mentioned operation modes are shown in Figure 1.2.

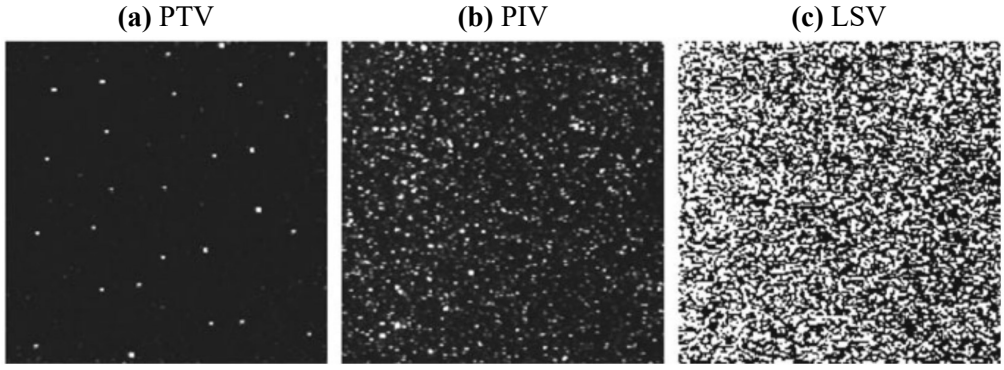

Figure 1.2 Low, medium, and high particle image density for different velocimetry operation modes. Adapted from [3]

In **Particle Image Velocimetry (PIV)** mode, tracer particles are seeded into the fluid flow and illuminated using a short-duration pulsed laser which causes the particles to scatter light. A camera, synchronized with the laser, captures an image with each laser pulse. The time delay between pulses is carefully adjusted based on the expected velocity range: shorter intervals are used for higher velocities, while longer intervals are suitable for lower velocities.

Once a pair of images is acquired, they are compared to detect the displacement of the particles over the given time interval, allowing the velocity field to be calculated [16, 17].

To calculate the velocity, the particle image is divided into small interrogation windows, for example, 32 × 32 pixels or enough to comply with the quarter rule. This rule states that the particle displacement should not exceed a quarter of the window size to ensure accurate cross-correlation results [2]. Cross-correlation is the technique used to identify the position of the same particles within corresponding interrogation windows in both images, enabling the measurement of their displacement between successive frames. Finally, by knowing the time interval between frames and the particle displacement, the velocity components in the x and y directions can be calculated for a 2D case. Additionally, stereoscopic PIV, which requires two cameras positioned at different observation angles, captures the out-of-plane z component of velocity, resulting in the simultaneous acquisition of 3 components of velocity (x, y, z) in a 2D plane. Tomographic PIV requires 3 or 4 cameras to capture 3 components of velocity (x, y, z) in a 3D volume [18]. Figure 1.3 shows a commonly used experimental arrangement for planar PIV.

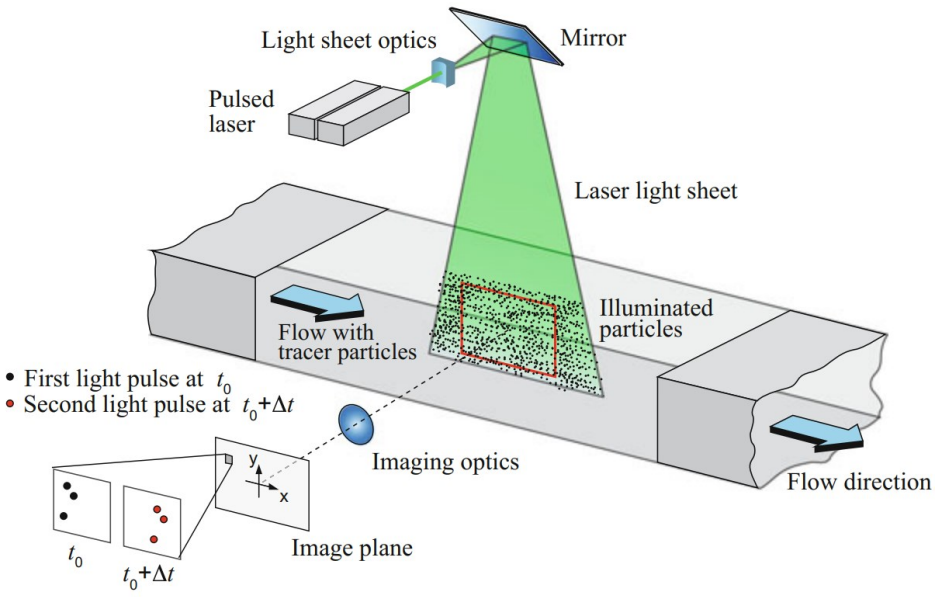

Figure 1.3 Typical PIV set-up for 2D PIV in a wind tunnel [3]

On the other hand, **Particle Tracking Velocimetry (PTV)** is a Lagrangian velocity measurement technique rather than an Eulerian technique as in PIV. In this method, particles are illuminated using either a pulsed laser or a continuous light source. The camera records a sequence of consecutive frames at constant temporal intervals, creating an image sequence that tracks the movement of particles over time. Unlike PIV, which captures pairs of images

separated by a short time delay, PTV tracks particles across multiple successive frames, allowing for the reconstruction of their trajectories. As shown in Figure 1.2, the particle seeding density is significantly lower than in PIV, ensuring that the particles remain well-separated and do not overlap in the images. As a result, individual particles are tracked directly, rather than relying on cross-correlation techniques as in PIV [19]. However, this methodology is less suitable for turbulent flows or cases requiring the identification of fine flow structures or high spatial resolution. Due to the lower particle image density, fewer velocity vectors or particle tracks are available, making it more challenging to resolve both large and small scale structures in the flow field [3].

When the particle image density is very high (typically with a source density $N_s > 1$ which is the expected fraction of the image plane covered by particle images [2]), individual particle images overlap and produce interference patterns known as speckle. This condition defines the **Laser Speckle Velocimetry (LSV)** regime. However, speckles tend to change their appearance when the displacement is large, which can lead to image decorrelation and make the evaluation more difficult [3].

1.3 Frame-Based Cameras

Conventional imaging systems used in most applications capture full images (frames) at fixed time intervals. These frame-based cameras are equipped with a lens that focuses light onto the sensor of the camera, which consists of a 2D array of pixels. Each pixel in the sensor contains a photodetector that measures the intensity of the incoming light and converts it into an electrical signal, which is later transformed into a digital value used to construct the final image. Every time the camera takes a picture, the shutter opens for a specified exposure time, allowing light to reach the sensor. Once the exposure ends, the shutter closes, and the data from the sensor is transferred to the memory during a process called readout [20]. The data is collected synchronously from all pixels to form an image, as shown in Figure 1.4.

During the readout process, the sensor is temporarily unable to capture new information, leading to a potential loss of data, particularly if motion or significant changes occur in the camera's field of view during this period. As shown in Figure 1.4, each frame is captured during an exposure window when the shutter is open and light is collected. After each exposure, there is a brief period of time when the shutter is closed, and the sensor is reading out the data. During this time, no new light information is being recorded. These intervals between exposures create temporal gaps between frames, which can result in motion being missed or inaccuracies, especially when tracking fast-moving objects [22, 23].

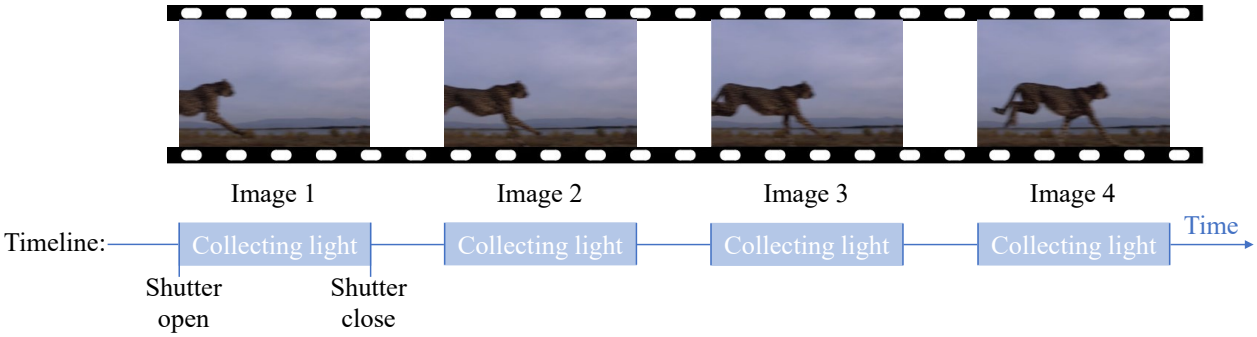

Figure 1.4 Principle of operation of a frame-based camera. Adapted From [21]

The frequency at which frames are captured and read out is called the frame rate, measured in frames per second (fps). This parameter is critical for image clarity and motion precision. The frame rate is typically fixed, and it limits the camera's ability to resolve fast-moving scenes, as the performance of the sensor is constrained by the frame rate rather than the dynamics of the observed scene [22].

Another important parameter in frame-based imaging is the exposure time, which directly affects image sharpness. It refers to the duration the sensor collects light during each frame. When an object moves significantly during this period, the resulting image can appear blurry. Using shorter exposure times helps to minimize this effect, producing sharper images of fast-moving objects [20].

Although short exposure times are not inherently tied to high frame rates, high-speed cameras typically use both high frame rates and short exposures to capture fast motion effectively. At high frame rates, the maximum allowable exposure time per frame is limited by the frame rate. For instance at 1000 fps the maximum exposure time is 1 ms. Often, high speed camera manufacturers set the exposure time by default within the control software, however acquisition rate and exposure time are two distinct concepts.

Figure 1.5 shows an example of how decreasing the exposure time as the frame rate increases leads to reduced motion blur and therefore improves the sharpness of a fast-moving object.

A major limitation of frame-based cameras is that all pixels capture information simultaneously, which leads to data redundancy. For example, in Figure 1.4, the static sky region appears identical across multiple frames, but the camera records this unchanging scene repeatedly, consuming memory unnecessarily. This inefficiency becomes especially problematic when only small portions of the scene are dynamic while most of the image remains static, leading to inefficient use of storage and processing resources.

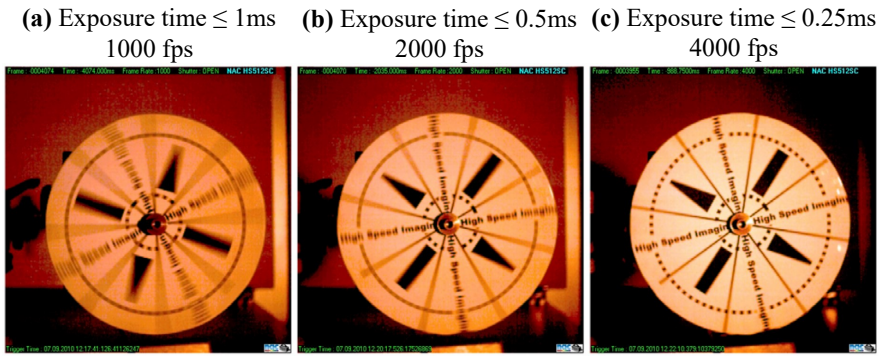

Figure 1.5 Impact of exposure time on motion blur during high-speed imaging of a target rotating at 25 Hz. The sharpness improves with decreasing exposure time from (a) $\leq$ 1 ms to (b) $\leq$ 0.5 ms to (c) $\leq$ 0.25 ms. Adapted from [20]

1.4 Event-Based Cameras

The creation of event-based cameras was motivated by the limitations of conventional frame-based systems and the efficiency of biological vision. Unlike conventional cameras, which capture entire frames at fixed intervals, event cameras are inspired by the way the human retina processes information by detecting changes in light intensity at each pixel independently. This bio-inspired approach offers several advantages.

1.4.1 Bio-Inspired Design and Principle of Operation

According to Mead (1990) [7], biological systems process information more efficiently by using relative variations in analog signals instead of the absolute values of digital signals. This principle, applied to neuromorphic circuits, makes them significantly more efficient in terms of both power and the amount of silicon material usage, which translates into lower production and operational costs. Experimental results have shown that adaptive analog systems can consume up to 10,000 times less power and require 100 times less silicon area than comparable digital systems, while also being more resistant to component degradation.

In Figure 1.6 we observe the circuit of an event camera pixel and how it compared to its biological inspiration, the human retina. The circuit consists of three main sections, each one corresponds to a stage of the retina's processing pathway:

1. **Photoreceptor Stage:** In the biological retina, rods and cones detect incoming light and convert it into electrical signals. Similarly, in an event camera, light intensity is detected by a photodiode, which generates a photocurrent (I_{ph}). This current is

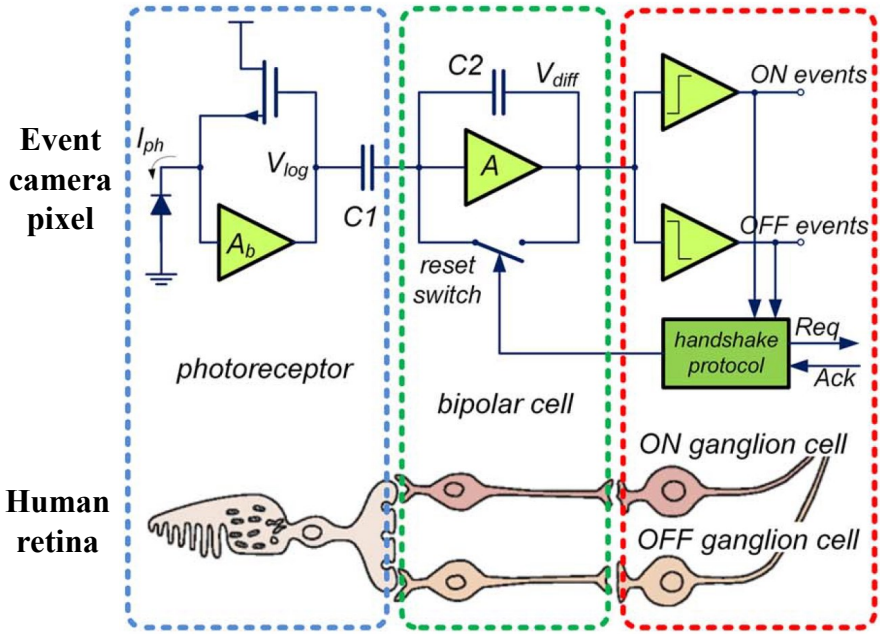

Figure 1.6 Event camera pixel circuit compared to human retina. Adapted from [24]

then converted into a voltage ($V_{\log}$) that is proportional to the logarithm of the light intensity.

2. **Contrast Detection Stage:** In the retina, bipolar cells receive signals from the photoreceptors and detect contrast by comparing their signals with those of surrounding cells. ON bipolar cells activate in response to brightening, while OFF bipolar cells activate in response to darkening. In the event camera circuit, this contrast detection is performed by an amplifier (A), which processes the voltage received from the photoreceptor and compares it to a reference level (V_{diff}).

3. **Spike Generation and Transmission:** In the retina, ON and OFF ganglion cells receive input from their respective bipolar cells and send spike signals through the optic nerve to the brain. Similarly, in the event camera circuit, ON and OFF events are generated when the light intensity increases or decreases, respectively. These events are transmitted via a handshake protocol, where the request (Req) and acknowledgment (Ack) signals ensure reliable data transfer, similar to how ganglion cells transmit spikes to the visual cortex [24].

A temporal intensity contrast $C(t)$ is defined as:

$$C(t) = \frac{\ln I(t) - \ln I(t_{\text{p}})}{\ln I(t_{\text{p}})}$$

where $I(t)$ is the intensity in the current time and $I(t_p)$ the intensity at the previous event [25].

The event-camera user specifies a contrast threshold C_{thld} to which is compared $C(t)$ (this is equivalent to specifying V_{diff} in Figure 1.6). If $C(t) > C_{thld}$, an ON event is generated. If $C(t) < -C_{thld}$, an OFF event is generated. A sequence of such events on a $\ln I(t)$ vs. t plot is shown in Figure 1.7.

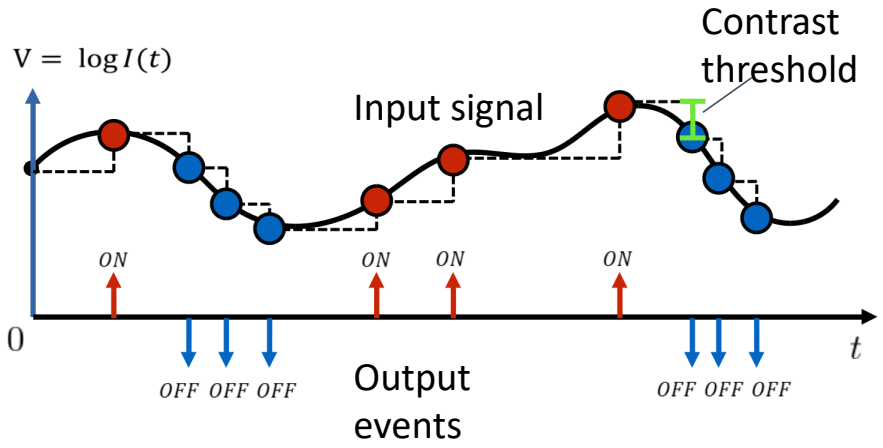

Figure 1.7 Principle of event generation in an event camera [26]

Each event is represented by four columns:

- the **x** position of the pixel where the event was triggered,
- the **y** position of the pixel where the event was triggered,
- the timestamp in microseconds (µs), indicating the precise moment the event occurred, and
- the polarity, which specifies the direction of the light change: 1 for a positive change (ON event) and 0 for a negative change (OFF event).

The theoretical temporal precision of event camera pixels is 1 µs, meaning the photoreceptor samples the light intensity every 1 µs and generates a corresponding voltage signal. However, this does not mean that an event is triggered every microsecond; an event is only generated if the contrast threshold condition is met. In contrast, frame-based cameras have a fixed temporal resolution determined by their frame rate, capturing and storing images at regular intervals, even when no changes occur in the scene.

Figure 1.8 illustrates the output from both types of cameras when recording the same scene. In traditional imaging, the output consists of frames, while the event camera generates ON

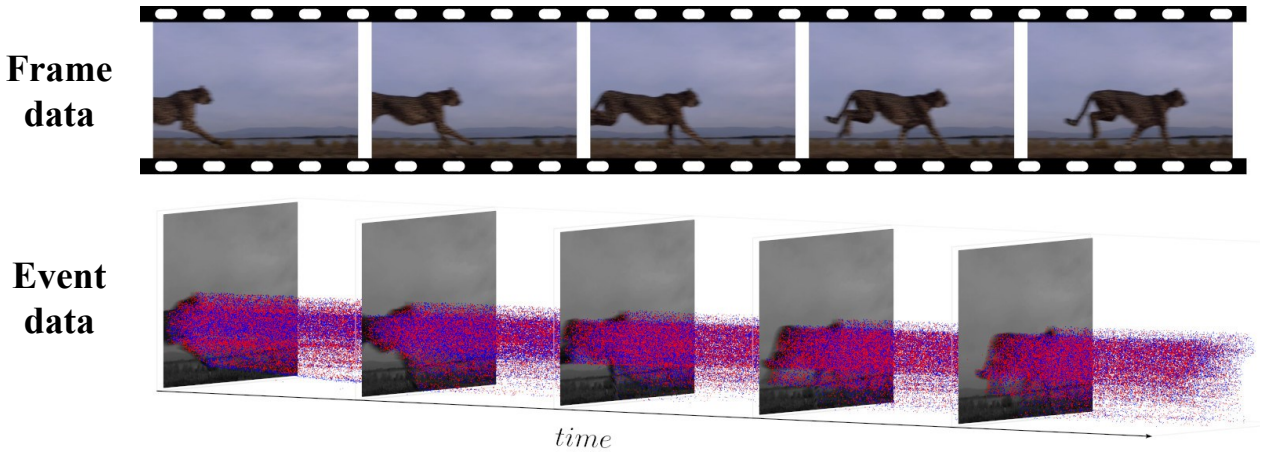

Figure 1.8 Visual comparison between the output of a conventional frame-based camera (top) and an event-based camera (bottom) tracking a fast-moving object. Adapted From [21]

(red) and OFF (blue) events. Events are displayed in spatio-temporal space, where both the position and time of occurrence are represented, whereas frames are shown in 2D space, only capturing spatial information at fixed time intervals.

Due to these differences in output format, one of the main challenges of event cameras is developing techniques for high-level processing of event-based data, a field that is still evolving [27]. Nevertheless, research into event camera sensors and their application scope has been steadily growing over the years [28].

The previously described characteristics of event cameras give them several advantages over frame-based cameras, including:

- **Low power consumption:** Event cameras avoid redundant data collection by only processing active pixels where changes in illumination occur. This selective processing significantly reduces power usage compared to frame-based cameras, which capture and process entire frames regardless of changes.
- **High dynamic range (HDR):** Event cameras can simultaneously detect both bright and dark stimuli within the same scene, offering a significantly higher dynamic range than traditional cameras. While standard cameras typically have a dynamic range of around 60 dB, event cameras can achieve values exceeding 120 dB [28], ensuring robust perception in challenging lighting conditions.
- **Microsecond temporal resolution:** Event cameras operate with a 1 MHz clock, enabling them to capture events with microsecond precision. This capability makes

them highly effective for recording high-speed motion, as they can detect rapid changes with minimal temporal delay.

- **No motion blur:** Since event cameras capture information asynchronously and instantly upon detecting changes, they are immune to motion blur. In contrast, frame-based cameras are prone to blur when objects move significantly during a single exposure.

Depending on the application, some features such as latency may be either advantageous or limiting, especially when compared to high-speed cameras used in fluid diagnostics. In this context we find the following limitations:

- **Resolution:** Recent event camera models offer a maximum spatial resolution of 1280 $\times$ 720 pixels [29], which is generally lower than most high-speed cameras. This can limit the ability to resolve the finer spatial length scales in complex flows, which is particularly important for quantitative measurements in experimental fluid mechanics such as Particle Image Velocimetry (PIV) or Particle Tracking Velocimetry (PTV).
- **Latency:** Although event cameras offer microsecond-level temporal resolution, the actual latency, which is the time between event detection and readout, is constrained by the camera's internal architecture and scene being recorded. For many models, this readout latency is roughly 200 µs [29], but it can vary considerably depending on the experimental conditions, as demonstrated in [30]. While acceptable in many robotics and surveillance tasks, this latency can be a drawback in experimental fluid velocimetry, where conventional high-speed cameras offer lower latency and more consistent acquisition timing.
- **Bandwidth:** Event cameras have a limited capacity to process events per unit of time. According to manufacturers, modern sensors can handle up to 1066 Mevps (million events per second) [28]. However, bandwidth can become a limiting factor when handling "busy scenes" [9], which is when a scene generates a high volume of events in a short period, for example, during a PIV recording with high particle image density. In such cases, the bandwidth limit may be exceeded, leading to saturation effects, which manifest as data loss, specifically missing rows of data.

1.4.2 Read-out Process

Latency and bandwidth limitations in event cameras are linked to the readout architecture of the sensor, which is illustrated in Figure 1.9. This figure presents a simplified schematic of

the chip block diagram showing the readout system for a 1280 × 720 pixel array, proposed by Finateu et al. [12]. It shows how individual events are propagated through a chain of interfaces before reaching the digital output pipeline.

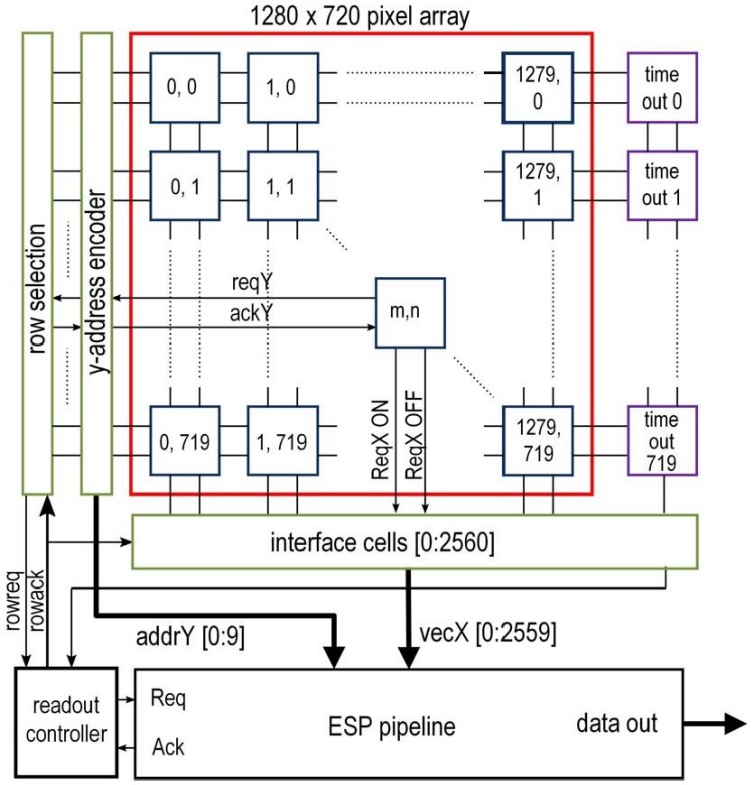

Figure 1.9 Chip block diagram illustrating the readout architecture of an event camera [12]

When a pixel generates an event, it sends a row request signal (reqY) to the Y-interface, which is composed by the Y-address encoder and row selection blocks in Figure 1.9, to initiate processing for its row. The Y-interface contains an arbiter, which manages the incoming requests following the first in, first out (FIFO) principle, ensuring that events are processed in the order they arrive. Once the request is granted, the Y-interface activates a scanning signal for the selected row (ackY). During this step, all pixels in the selected row can send an X-request if they have detected an event, either ON (reqX ON) or OFF (reqX OFF), depending on the event's polarity, indicating its X-address. The signals from the Y address (row being processed), along with all the X-address (active pixels in that row) are collected by the interface cells and then transferred to the Event signal processing (ESP) digital pipeline, where they are assigned a timestamp. Because the row is processed as a unit, all events scanned at that time within that row share the same timestamp. Finally, the process repeats, moving on to the next row for event readout.

Since rows are processed sequentially, meaning that pixels in other rows must wait before their events are read out. When many events occur simultaneously, this waiting time increases, which can be observed in the timestamps of rows that waited for a long time to be processed. This effect, known as readout delay or **latency**, is the time between when an event is generated and when it is actually recorded, and is the first limitation identified in the readout of event cameras.

When the number of events occurring simultaneously exceeds a threshold known as the **bandwidth**, the camera becomes unable to process all the events, leading to data loss. This constitutes the second limitation identified in the readout system. Since the readout is performed row by row, as previously described, this data loss manifests as missing or unprocessed rows, an effect often referred to as readout saturation.

In the latest sensor generations, significant improvements have been achieved [29], with reduced latency and increased bandwidth, and further advancements are expected to continue addressing these limitations in future designs.

1.5 Particle Velocimetry with Event-Based Cameras

This section presents a comprehensive review of the main studies on event-based particle velocimetry, covering both particle image velocimetry (PIV) and particle tracking velocimetry (PTV) approaches. The works are organized by methodological similarities, highlighting the evolution of techniques, camera technologies, and experimental strategies. For each group, we examine the methodology, achievements, and limitations. This analysis not only traces the development of event-based velocimetry but also identifies current challenges and emerging trends in the field.

Table 1.1 provides a summary of all the studies that will be covered in this section, with an overview of the test conditions and key details of each experimental setup.

Table 1.1 Event-Based Particle Velocimetry Summary

Authors	**Camera**	**Flow Type**	**Velocity range**	**Seeding**	**Illumination**	**Validation**
Planar Event-Based Particle Tracking Velocimetry						
Drazen et al. 2011 [31]	DVS128	Turbulent - Water	0.22 to 2.04 m/s	950 µm polystyrene particles - 1.02 g/cm^3	5W Innova 300C multi-line argon-ion laser	Photron Ultima APX frame camera

Howell et al. 2020 [32]	CSD3SHCD Prophesee	Laminar - Phosphate-buffered saline solution	0.04 to 1.54 m/s	1 and 10 µm fluorescent polystyrene beads - $1 \times 10^4 - 5 \times 10^5$ beads/mL	Fluorescence microscope standard illumination	DinoLite frame-based camera
3D Event-Based Particle Tracking Velocimetry						
Borer et al. 2017 [33]	DVS128	Not specified - Air	0.5 to 17 m/s	Milimeter-sized helium-filled soap bubbles - 10 bubbles/s	LED lamps	-
Wang et al. 2020 [34]	PEK3SHEM Sensor: CSD3SVCD Prophesee	Not specified - Water	5 to 20 rad/s simulated data and 0.3 - 72.4 mm/s exp.	90 to 106 µm polyethylene microspheres - 0.006 to 0.03 ppp simulated data	Collimated light	Synthetic data with known ground truth motion fields
Rusch et Rösgen 2023 [35]	Not specified	Turbulent - Air	5 to 60 m/s	Helium-filled soap bubbles	LED arrays	-
Willert et Klinner 2025 [36]	EVK4 Prophesee, Sensor: IMX636 Sony	Turbulent boundary layer - Air	5.2 to 10 m/s	1-2 µm water-based tracer particles	5 kHz pulsed laser (Innolas/Iradion Nanio-Air 532-10-V-SP)	Direct Numerical Simulations (DNS)
Event-Based Particle Image Velocimetry (PIV)						
Willert et Klinner 2022 [25]	**SilkyEvCam** PPS3MVCD Prophesee and **EVK2-HD** Prophesee	Turbulent - Water and Air	Up to 1.5 m/s	10 µm silver coated glass spheres and 1 µm parafin droplets	Continuous-wave laser (Kvant Laser, 4–5.6 W, 520 nm)	-

Willert 2023 [37]	EVK2-HD Prophesee Gen 4	Laminar and Turbulent - Water and Air	1.5 to 3 m/s	10 µm silver coated glass spheres - 0.0033 to 0.0153 ppp	5.2 W, 450 nm laser pulsed at 500 Hz–20 kHz (NEJE Tool E30130)	PixelFly-PIV frame camera
Raffel et al. 2024 [38]	EVK2 Prophesee	Not specified - Air	1 m/s	1 µm paraffin droplets	50 nm pulsed laser (NEJE Tool E30130) at 5 kHz	-
Franceschelli et al. 2025 [39]	EVK4-HD Prophesee, Sensor: IMX636 Sony	Turbulent - Water and Air	0.13 and 2.8 m/s	Polyamide particles and paraffin droplets	Pulsed LaserTree LT-40W-AA	Andor Zyla sCMOS camera and Phantom T4040 camera
Cao et al. 2025 [30]	EVK4 Prophesee	Laminar and Turbulent - Water	1 m/s	50 µm polyamide particles - 0.0102 ppp and from 0.004 to 0.06 ppp (simulated data)	532 nm pulsed laser	DaHeng frame-based camera
New Developments in Event-Based Velocimetry						
AlSattam et al. 2024 [40]	EVK2 Prophesee	Not specified - Water	0 to 50k px/s simulated data and 0.28 m/s exp.	0.03 ppp	Continuous light laser	Synthetic data with known ground truth motion fields

AlSattam et al. 2024 [41]	EVK2 Prophesee	Not specified - Water	0 to 50k px/s simulated data and 0.28 m/s exp.	0.03 ppp	Continuous light laser	Synthetic data with known ground truth motion fields
Zeng et al. 2025 [42]	EVK4-HD Prophesee	Not specified (Re = 4400) - Water	0.22 m/s	50 µm polyamide particles - 0.0016 and 0.0063 ppp	Dual-laser setup (450 nm pulsed @ 2 kHz + 532 nm CW)	High-speed PCO CMOS camera

1.5.1 Planar Event-Based Particle Tracking Velocimetry

The first demonstrations of the use of event cameras for velocimetry were focused on particle tracking. The pioneering work by Drazen et al. (2011) [31] presented a proof of concept study to demonstrate the feasibility of using event cameras for tracking particles in fluid flows using a DVS 128 camera. In their experiment, a single event camera observed water flow inside a pipe, seeded with 950 µm polystyrene particles. The illumination was provided by a 5 W Innova 300C multiline argon-ion laser and the tested flow velocities ranged from 0.22 m/s to 2.04 m/s, corresponding to Reynolds numbers (Re) between 11950 and 108780. The camera's performance was validated using a conventional high-speed Photron Ultima APX frame camera. A key observation was that the event camera required relatively high contrast for effective detection, which led to missed low-contrast particles. Nevertheless, the spatial accuracy of the tracked particle positions was consistent with that of the frame-based system. A significant advantage was the reduced data size, with only 840 kB recorded for a 6-second event stream compared to 120 MB (or 0.7%) from conventional imaging.

Howell et al. (2020) [32] extended event-based PTV to microfluidic applications. They used a CSD3SHCD Prophesee camera mounted on a fluorescence microscope with standard illumination to track a flow seeded with fluorescent polystyrene beads in a phosphate-buffered saline solution within a spiral microfluidic channel. The tested velocities ranged from 0.04 to 1.54 m/s (Re = 4 - 159) and for validation they used a DinoLite frame-based camera. Particle detection was demonstrated up to 1.54 m/s and good tracking performance up to 0.4 m/s using a Kalman filter combined with the Munkres algorithm. The study demonstrated compatibility of event cameras with microscopy setups, but also pointed to the need for improved processing frameworks tailored for microfluidic conditions. Together, these studies laid the foundation for applying event-based sensors in both macro- and micro-scale PTV,

while highlighting key challenges such as contrast requirements, velocity limits for tracking, and algorithmic development needs.

1.5.2 3D Event-Based Particle Tracking Velocimetry

Several studies have extended event-based particle tracking to three dimensions using synchronized multi-camera setups. Among the earliest, Borer et al. (2017) [33] demonstrated 3D tracking using three synchronized DVS128 event cameras observing an Ahmed body (a simplified car-shaped model) in a wind tunnel seeded with helium-filled soap bubbles. The illumination was provided by LED lamps, and the detected air velocities ranged from 0.5 to 17 m/s. They identified the need for a pre-filtering step to reduce noise in the event data and developed a custom pre-processing method to address it. The key contribution was the implementation of an extended Kalman filter for 3D particle tracking and flow visualization. However, they noted that higher flow velocities reduced the number of events per track due to pixel dead-time, ultimately decreasing track quality and limiting seeding density.

Similarly targeting 3D flow tracking but under more controlled conditions, Wang et al. (2020) [34] developed and validated a stereo PTV method using two synchronized event cameras. The method was first validated using synthetic data where rigid-body-like vortices were simulated for various angular velocities and particle densities. The method was also tested experimentally, using two PEK3SHEM Prophesee cameras set at a 60° angle. Their experimental setup involved a hexagonal water tank seeded with polyethylene microspheres and illuminated by a collimated light. Two types of flows were tested: vortices generated by a magnetic stirring rod and fluid injections using a syringe. The system handled a wide range of particle densities and flow velocities, 5-20 rad/s in synthetic simulations and 0.3-72.4 mm/s in experiments and achieved full 3D flow and velocity reconstruction with high temporal resolution, enabling visualization of complex flow structures. However, the method was limited by the low spatial resolution of current event cameras and bandwidth saturation at high flow speeds, which caused the system to fail when the vortex speed exceeded a certain threshold, not quantified by the authors.

Building on real-time capabilities, Rusch and Rösgen (2023) [35] introduced the TrackAER method, enabling real-time 3D PTV and flow visualization using multiple event cameras. Their experimental campaign included airflow around a car, a turbulent free jet, and wake measurements behind a delta wing model. All setups were seeded with helium-filled soap bubbles and illuminated using LED arrays. The method successfully captured complex vortex structures and transient flow behaviors in three dimensions. Velocity measurements from 5 to 60 m/s were achieved with an error margin of ±0.75–1.75%. However, at flow speeds above 60 m/s, tracer signal weakening reduced data quality, limiting performance and leading to

reconstruction failures.

All the studies discussed so far employed LED or continuous light sources for illumination, avoiding the use of lasers. This makes them particularly suitable for environments where laser usage is restricted or undesirable. In contrast, Willert and Klinner (2025) [36] advanced the state-of-the-art by implementing 3D Lagrangian Particle Tracking using pulsed laser illumination at 5 kHz. Three synchronized EVK4 cameras were used to study near-wall turbulent boundary layers in a wind tunnel at velocities of 5.2, 7.5, and 10 m/s seeded with 1–2 µm water-based tracers. Their setup achieved strong agreement with direct numerical simulations (DNS) in terms of wall shear stress statistics at similar Reynolds numbers, with optimal data quality observed at event rates of 8–12 $\times$ 10^6 events/s. Despite this success, high seeding densities degraded tracking accuracy, and spanwise wall-shear fluctuations were slightly underestimated due to sampling limitations near the wall.

1.5.3 Event-Based Particle Image Velocimetry

Several recent studies have extended the application of event cameras to Particle Image Velocimetry (PIV) which has progressed from early feasibility studies to detailed assessments of resolution, accuracy, and operational limitations. Willert and Klinner (2022) [25] contributed a comparative analysis of three event-based image velocimetry (EBIV) techniques: motion compensation, sum-of-correlation, and event-based PIV, the latter involving the reconstruction of pseudo-frames from event data for conventional PIV processing. Their experiments included a water tank with recirculating turbulent flow seeded with silver-coated glass spheres and a wind tunnel operating at 1.5 m/s (Re = 1400) seeded with 1 µm paraffin droplets. Illumination was provided by a continuous-wave laser (4–5.6 W, 520 nm) forming a 1 mm light sheet. They found a good agreement between the three EBIV techniques results with differences on the order of 0.1 pixels/ms. Importantly, they found reliable velocity detection up to 50,000 px/s and 50×10^6 events/s. However, in low-velocity regions, EBIV performance degraded due to insufficient event generation. Although temporal intensity variations such as flickering are generally undesirable, the authors suggest they might be repurposed to improve visibility of slow-moving particles.

Building on these insights, Willert (2023) [37] introduced pulsed illumination which addresses the limitation of low event generation in quiescent flow regions. The study evaluated pulsed-event-based image velocimetry (pulsed-EBIV) using the EVK2-HD prophesee camera in two experimental setups: a submerged water jet at 1.5 m/s seeded with coated glass spheres, and a wind tunnel test involving laminar and turbulent boundary layers over a square rib at 2 m/s. Seeding densities from 0.003 to 0.015 particles per pixel (ppp) were tested across different regions of interest. Illumination was provided by a 5.2 W, 450 nm pulsed laser

(NEJE Tool E30130) operated at frequencies ranging from 500 Hz to 20 kHz. A frame-based camera (PixelFly-PIV) was used for comparison. Pulsed-EBIV produced velocity fields comparable to those from traditional PIV. Pulsed illumination was found to reduce latency effects enabling clear separation of successive flow fields and enhanced event generation from stationary or slow-moving particles. Most events were captured within 150–200 µs, enabling reliable measurements at 5–7 kHz. Pulsed operation allowed velocity measurements beyond 200,000 px/s (e.g., 20 px displacement @ 10 kHz). However, the method is constrained by the sensor bandwidth, which experienced saturation with event rates beyond ∼40 Mev/s which can result in either limited resolution or particle image density.

Raffel et al. (2024) [38] explored the benefits of event-based sensing for PIV under in-line illumination conditions. They used an EVK camera to test a bluff-body wake in air at 3.5 m/s seeded with paraffin droplets and a 450 nm pulsed laser operating at 5 kHz. The camera system, which incorporated a light trap in front of the lens, demonstrated that event-based imaging could significantly extend the range of resolved flow length scale while reducing illumination requirements due to the high sensitivity of the sensor.

In a complementary direction to EBIV applications, Franceschelli et al. (2025) [39] evaluated the potential of event cameras for capturing low-order modes (dominant flow structures) in turbulent flows via EBIV. They performed two experiments: a submerged water jet at 0.13 m/s seeded with polyamide particles and illuminated by a pulsed LaserTree LT-40W-AA, and a channel airflow at 2.8 m/s around a square rib seeded with paraffin droplets and illuminated by a high-speed pulsed laser. Validation was performed against an Andor Zyla sCMOS and a Phantom T4040 camera, respectively. Their results showed that EBIV accurately captured flow statistics and dominant structures, despite higher noise levels compared to PIV. This noise led to increased total energy content and discrepancies at high frequencies, although low-order modes remained minimally affected. Notably, peak locking was observed due to the binary nature of pseudo-images, which limits sub-pixel resolution.

Finally, Cao et al. (2025) [30] studied the impact of particle size and concentration on EBIV acquisition rate using a digital micro-mirror device to simulate particles with constant-speed displacements. They used a beam splitter to enable both EVK4 Prophesee event camera and DaHeng frame-based camera to observe the same field of view (FOV). In addition to the simulated particles tests, a validation experiment was conducted using a water jet experiment in a tank seeded with 50 µm polyamide particles. Their findings provided practical guidelines for selecting particle size and concentration to minimize velocity uncertainty. Results showed that increasing particle size and concentration led to higher event rates and longer readout delays. However, for concentrations above 0.03 ppp, the readout delay stabilized around 420 µs, limiting the acquisition rate to 2.4 kHz. Beyond this threshold, a noticeable reduction in

event density was observed in certain rows, attributed to event overflow or sensor saturation. Despite these limitations, the experimental validation demonstrated that flow structures can be clearly captured at 4 kHz, and the flow fields reconstructed through the event-based camera showed good agreement with those from the frame-based PIV at 125 Hz, with a mean velocity uncertainty of 1.15%.

Together, these studies confirm the suitability of event cameras for PIV applications, especially when paired with pulsed illumination to mitigate latency and improve visibility. They also highlight challenges such as sensitivity to noise, readout delays at high particle concentrations, and lack of subpixel accuracy due to the binary nature of pseudo-images reconstructed from event data.

1.5.4 New Developments in Event-Based Particle Velocimetry

Recent efforts have explored strategies aimed at improving the accuracy and robustness of event-based velocimetry. AlSattam et al. (2024) [40,41] proposed Particle Event Velocimetry (PEV), an approach that estimates the flow field by detecting particle events in the asynchronous stream and tracking their trajectories over time. Unlike conventional frame-based PIV/PTV or earlier event-based PIV approaches, PEV achieves higher spatial resolution limited only by particle image density while also offering increased noise resilience.

Their initial study [40] validated the method using both synthetic and experimental data. The synthetic dataset modeled a forced vortex at 0.03 ppp with velocities up to 50,000 px/s, allowing quantitative comparisons with other event based and frame based methods. Experimentally, the method was tested in a horizontal water tunnel operating at 0.28 m/s under continuous laser illumination. PEV showed strong noise robustness and high accuracy in boundaries and flow curvatures. Particle velocities from 10 to 50,000 px/s were successfully reconstructed and outperformed other event-based algorithms in velocity reconstruction. The authors also emphasized its cost-effectiveness compared to traditional PIV/PTV setups, requiring less complex hardware. However, the method is unsuitable for real-time applications due to its non-causal design, which relies on processing future information to estimate current flow.

In a follow-up study, the same authors introduced a Kalman Filter-based variant of the algorithm (KF-PEV) [41], designed as a causal framework to overcome the non-causal limitations of the original method. The performance of this version was compared with their original PEV approach and other velocimetry methods using both synthetic data and experiments involving a horizontal water tunnel with an SD7003 airfoil at 0.28 m/s, tested at 0° and –8° angles of attack. KF-PEV achieved the most accurate and stable velocity reconstructions among the compared methods and produced denser velocity fields than the original

PEV. However, increased particle density introduced greater computational complexity and susceptibility to tracking errors. While KF-PEV enhanced robustness and marked a significant advance toward real-time, high-resolution event-based velocimetry, its implementation in practical scenarios is still constrained by computational cost, an aspect the authors intend to address in future developments.

In contrast to the previous approaches, which rely exclusively on event-based tracking, Zeng et al. (2025) [42] explored a hybrid method that combines both event and frame data to enhance particle tracking performance. They proposed a temporally adaptive PTV approach (TA-E-PTV) that fuses asynchronous data from an EVK4-HD event camera with synchronous frames from a 125 Hz DaHeng camera. The goal was to leverage the event camera's high temporal resolution while using the frame-based data to support particle detection and matching. The method was tested on a free jet in a water tank (Re = 4400) seeded with polyamide particles. To illuminate the field of view they used a dual laser set-up consisting in a 450 nm pulsed laser at 2 kHz and a 532 nm continuous-wave laser. A high-speed frame-based camera was used for reference validation. TA-E-PTV achieved effective temporal resolutions of up to 13.89 kHz at a seeding density of 0.0016 ppp and 7.69 kHz at 0.0063 ppp, with velocity estimates differing by less than 6% from the high-speed reference camera. This study offers a low-cost, high-precision alternative for particle velocimetry, and was shown to be particularly effective in flows with strong velocity gradients.

1.6 Research Scope

1.6.1 Knowledge Gap

In fluid velocimetry using event cameras, bandwidth and latency have been identified as the main limitations for measuring complex flows, particularly at high velocities and high particle image densities. Manufacturers have defined theoretical limits for these parameters, but these do not always reflect the actual behavior of event cameras in real experimental conditions. Some authors have identified specific event rate limits (e.g., C. Willert estimates 40–50 MEPS [25, 37]), yet according to manufacturers, these limits can vary significantly depending on multiple experimental factors like illumination, number of active pixels in the region of interest (ROI), spatial distribution events, camera orientation, focus adjustment, and other conditions [43].

Pulsed-PIV with event cameras has emerged as a promising alternative for velocity measurements in flows, as it does not require major modifications to traditional PIV methodology. Instead, just one additional processing step, which is to convert event-based data into pseudo-frames, is needed. This makes pulsed-EBIV, as it is referred to by the research community, a viable option for integrating event cameras into experimental fluid dynamics. However,

to effectively implement this approach, it is crucial to first characterize key experimental parameters that influence measurement uncertainty.
One such factor is the time between laser pulses, which determines the temporal resolution of the system and the dynamic velocity range that can be captured through PIV. This resolution is constrained by the readout latency of the camera, a parameter that has already been identified as dependent on the event rate (the number of events generated per microsecond). Another factor is the particle image density, which strongly influences the quality of the reconstructed velocity field and can be limited by the bandwidth of the camera.
In addition to these factors, other parameters influence the event rate, which impact latency and consume the available bandwidth in event-based PIV measurements. These include laser fluence, which affects particle contrast; particle image size, which depends on seeding and optics; and the camera's contrast threshold, which controls sensitivity to intensity changes. The study of experimental fluid dynamics using pulsed PIV with event cameras strongly requires a systematic evaluation of these parameters to better define their practical operating limits.

1.6.2 Research Objectives

The objective of this research is to develop a methodology to evaluate the performance of event-based cameras in measuring velocity in fluid flows using Particle Image Velocimetry (PIV). This study aims to establish the experimental conditions under which event cameras can be effectively used for PIV and define their limitations in terms of event rate, temporal resolution, and velocity measurement capabilities. The specific objectives of this research are:

1. Design and implement an experimental setup to characterize how latency and bandwidth affect the maximum event rate and temporal resolution achievable with an event camera.

2. Establish practical guidelines for users by determining the maximum event rate for a given velocity range and identifying the highest measurable velocity based on the camera's specifications.

3. Demonstrate the applicability of event cameras for velocity measurements in different types of fluid flows and compare their performance against conventional frame-based PIV cameras.

4. Investigate the influence of key PIV setup parameters—such as laser energy, particle image density, and particle image size—on the accuracy and reliability of event camera

measurements.

1.6.3 Structure of the Thesis

To achieve the proposed objectives, this thesis follows a paper-based format. The core of this work is presented in the research paper titled “An Evaluation of Event-Based Cameras for Particle Image Velocimetry”, which is included as a dedicated chapter under the same name. This paper provides a comprehensive study on the performance of event cameras for PIV, detailing the experimental methods, data analysis, and key findings. The final chapter presents the conclusions, summarizing the main contributions of this work and outlining potential directions for future research.

CHAPTER 2 ARTICLE 1: AN EVALUATION OF EVENT-BASED CAMERAS FOR PARTICLE IMAGE VELOCIMETRY

Luisa Maya[a,b], Luming Fan[c,a], Antoine Durocher[a], Bruno Savard[b], Patrizio Vena[a,b,*]

[a] Aerospace Research Centre, National Research Council, 1200 Montreal Road, Ottawa, ON K1A 0R6, Canada

[b] Department of Mechanical Engineering, Polytechnique Montréal, 2500 Chem. de Polytechnique, Montréal, QC H3T 1J4, Canada

[c] School of Aeronautics and Astronautics, Shanghai Jiao Tong University, 800 Dongchuan Road, Shanghai, 200240, P.R. China

Submitted to: *Experiments in Fluids*, July 8, 2025

Author contribution: Luisa Maya set up, tested, and characterized the measurement equipment; performed the experiments, uncertainty analysis, data processing, and initial data analysis; and wrote the first draft of the manuscript. Luming Fan supported the set up, experiments, data processing, initial data analysis, and contributed to the first draft of the manuscript. Antoine Durocher supported the set up and experiments. Luming Fan, Bruno Savard, and Patrizio Vena conceptualized the study. The theory development, final data analysis, and editing and revision of the manuscript were conducted jointly by Luisa Maya, Luming Fan, Antoine Durocher, Bruno Savard, and Patrizio Vena.

Abstract

Event-based cameras are dynamic vision sensors that provide a unique imaging approach, which differs from conventional frame-based cameras; they operate each pixel independently and only output a signal for changes in light intensity exceeding a user set threshold. High data efficiency is one of the advantages of this new technology, which is very attractive for applications that involve sparse/discrete signals like particle image velocimetry (PIV). Previous studies have demonstrated the application of event cameras in conventional pulsed PIV measurements, yet the impact of key hardware limitations in the state-of-the-art event cameras, specifically, latency and data bandwidth, on the velocity dynamic range has not been thoroughly investigated. In the first part of this study, we investigate the role of latency and information loss due to the bandwidth limit of the event camera on temporal resolution for pulsed PIV. We also study systematically the effects of the laser pulse energy, particle image density, particle image size and event triggering contrast threshold, by running single-pulse

planar illumination in a uniformly seeded water cuvette. In the second part, double-pulse event-based PIV is conducted in an air jet, in order to investigate the velocity dynamic range that can be achieved by the event camera. For all the experiments, an sCMOs PIV camera was set to capture the same particle images simultaneously with the event camera, to enable direct comparison between the event-based and framed-based PIV. Our findings indicate that, under the studied conditions, the event camera can record up to ~ 400 events per microsecond (ev/μs) without experiencing non-retrievable information loss. However, the camera's ability to measure velocity using PIV is constrained by latency, which increases proportionally with the event rate. This introduces a complex trade-off between particle image density, pulse interval, and the maximum detectable velocity. We identify an optimal range of particle image density, expressed in particles per pixel (ppp) for PTV and PIV based on both the available literature and the experimental results. In our air jet experiments, a 0.2-1.8 m/s (0.003-0.03 px/μs) velocity dynamic range is achieved for a robust cross-correlation using a typical 32×32 interrogation window. The PIV calculation showed good results for particle image densities above 0.018 ppp with uncertainties remaining below 0.4 px. The methodology introduced in this study can be readily applied to evaluate future event-based cameras with improved bandwidth and reduced latency, which would enable a broader velocity dynamic range and enhanced spatial resolution.

2.1 Introduction

Non-invasive flow visualization is an essential tool in experimental fluid dynamics, with a wide range of applications such as energy, transportation, industry, and biomedical science. Among the various laser diagnostics, Particle Image Velocimetry (PIV) is the most wide-spread and commonly used. Tracer particles are uniformly seeded in the flow and illuminated with two or more laser pulses to track their instantaneous positions. By measuring their displacement over a known time interval, the velocity field is determined [17]. While PIV is a powerful tool, it can 1) become relatively expensive, especially for temporally-resolved measurements that require costly high-speed lasers and cameras; and 2) result in significant data storage requirements, despite most of the captured data often consisting of non-useful information on the static background [24]. For instance, one double-frame PIV image captured by a 16 bit 2560×2160 pixels scientific Complementary Metal–Oxide–Semiconductor (sCMOS) camera can take several tens of MB of storage space, which doubles and even quadruples for stereoscopic or tomographic configurations with multiple cameras.

Event-based cameras, also known as neuromorphic cameras, are an emerging technology that may address these challenges. Unlike traditional frame-based cameras, which acquire and save all pixels on the sensor simultaneously and at a fixed frame rate, event cameras operate

asynchronously, recording changes in light intensity independently at each pixel [28]. The architecture of each pixel is composed of a rapid logarithmic photoreceptor circuit, a high-precision differencing circuit to detect and amplify variations in light intensity, and efficient two-transistor comparators, as detailed in [44]. "Events" are triggered only at individual pixels observing a change (in logarithm scale) in light intensity greater than a user defined contrast threshold. Following the definition in [25], the intensity contrast is calculated at each pixel as follows:

$$C(t) = \frac{\ln I(t) - \ln I(t_{\mathrm{p}})}{\ln I(t_{\mathrm{p}})} \tag{2.1}$$

where $I(t)$ represents the light intensity captured by the pixel at the current time t, and $I(t_{\mathrm{p}})$ corresponds to the intensity at time t_{p}, which is when the previous event occurred at the same pixel. An event is triggered whenever the absolute value of this intensity contrast $|C(t)|$ exceeds a preset threshold, typically expressed as a percentage.

After generating an event, individual pixels in the chip block enter the sensor's readout process to communicate the events through a readout interface. Rows are selected to be processed under the arbitration principle of First-In, First-Out (FIFO) [45], and then, active row events are assigned a timestamp and organized into a bit-efficient vector format for readout, as further described in [12]. However, when a high volume of events is generated simultaneously, the rows being processed start to experience a loss of timestamp because the arbiters cannot handle the number of events promptly. This loss of timestamp in the read-out process, combined with the on-pixel delay is know as global latency, which is the overall time delay between the occurrence of a real-world stimulus and the assigned timestamp to the corresponding event [37]. When the cameras's bandwidth limit is reached, the arbiters become saturated (known as readout saturation), which leads to a row-wise data dropout and the loss of information [37], where rows of events can be skipped or unrecorded, as described in [46]).

The output of an event camera is typically formatted to four columns; the pixel position (x, y), timestamp, and polarity (ON or OFF). Positive (ON) events correspond to an increase in intensity, and negative (OFF) events correspond to a decrease. As a result, event cameras only record objects that are in motion or changing brightness over time, whereas static elements are not recorded. This improves data efficiency and enables real-time data transport and processing, making event cameras a promising tool in application scenarios such as autopiloting and object tracking [47–49], and real-time 3D reconstruction [50, 51]. For the same reason, they are also particularly interesting for particle image velocimetry since the unchanged dark background will not be recorded, greatly reducing data size. In a wider scope of flow visualization, event-based cameras have been successfully applied to perform optical

flow estimation [52,53], image reconstruction [54–56], and back illumination Schlieren [57,58]. Another advantage of event cameras is their high temporal resolution. The theoretical response time can be as fast as 1 μs [28], which leads to a theoretical maximum data sampling rate up to 10^6 hertz at each pixel. Practically, limited by the readout data bandwidth, current state-of-the-art event cameras can achieve an equivalent maximum sampling rate around 5 kHz [37]. Compared with a commercial high-speed sCMOS camera that can achieve a similar frame rate, the event cameras are significantly less expensive, smaller, and lighter, which also adds to the appeal. For example, event cameras can be integrated into lightweight drones [59, 60], where traditional high-speed cameras would be too large or heavy to even consider. Additionally, their affordability could enable the use of multi-camera set-ups for stereo/tomo PIV at a significantly lower cost.

Drazen et al. [31] were among the first to investigate particle detection using event cameras. They presented a proof-of-concept study by comparing the performance of an event camera with a high-speed CMOS camera. In terms of efficiency, they highlighted that only 840 kB were needed to store data from the event camera, compared to 120 MB for the CMOS at an equivalent spatial resolution, both recording the same sequence during 6 seconds, with the CMOS at 2000 fps. Efforts to develop methods for 3D fluid flow reconstruction through Particle Tracking Velocimetry (PTV) using event cameras have been made by [33–35] demonstrating that multiple event cameras can be operated at different viewing angles to recover 3D particle trajectories and velocity fields. Based on those studies, PTV shows significant promise for event-based velocimetry due to its continuous recording nature [54]. However, because event cameras produce asynchronous data, in contrast with sCMOS cameras, novel algorithms to resolve stereo-vision in 3D space are needed [28], which remains an active topic of research in computer vision science [61].

Willert and Klinner [25] successfully demonstrated in-plane event-based PIV using a continuous wave (CW) laser. They observed that under continuous illumination, when the velocity in the field of view is not homogeneous, information about slower particles is often inadequate and insufficient for an accurate velocity calculation. In subsequent work, Willert then pursued pulsed-PIV with event cameras [37], by illuminating a seeded water cuvette flow with a pulse width modulation (PWM) laser at frequencies between 500 Hz and 20 kHz to quantify event latency. They found that most of the events associated with the laser pulse were captured within 150-200 μs for a full sensor resolution and operating below the arbiters saturation event rate, which they estimated to be 40×10^6 events/s for the camera used (corresponding to pulsing rates of 5-7 kHz). They introduced a methodology called Event Based Image Velocimetry (EBIV), where two-dimensional "pseudo-images" are reconstructed by accumulating events along the time axis, enabling the use of cross-correlation-based PIV

algorithms for analysis. This approach has been applied in several studies, including [39, 62]. Despite successful demonstrations of event-based PIV and PTV, several limitations associated with the hardware remain. First, the limited data bandwidth, which is the capacity of the camera's read-out interface hardware to process a large amount of events at the same time, may be easily exceeded when observing a highly dynamic scene [44]. For PIV, this translates to limiting the seeding density in the flow, and the camera's projected spatial resolution within the analysis region of interest, ultimately affecting the quality of the cross-correlation. Second, the latency imposes an implicit limit on the minimum time interval between laser pulses, with values up to $\sim$ 200 μs reported in the camera's specifications [12]. This, in turn, limits the maximum velocity that can be measured for a given spatial resolution. As summarized in [37], the event camera's latency may even be higher than 200 μs and depends on lighting conditions, various adjustable detector parameters, and the number of events per unit time.

Although previous studies have reported on these challenges/limitations, a systematic evaluation of the effect of key parameters such as laser energy, particle image density, particle image size, and contrast threshold remains critically important to ensure the continued and effective implementation of EBIV. To address this, characterization experiments are first conducted using a water/alumina suspension flowing in a cuvette. Assessing the event camera's response to a single laser pulse, the effect of latency and potential information loss on the effective temporal resolution of pulsed PIV measurements is investigated. The effects of the laser pulse energy, particle image density, particle image size, and contrast threshold are also evaluated systematically. Using this methodology, a performance map of the event camera is generated, serving as a tool for users to determine optimal configurations and parameters for PIV measurements. In a second set of experiments, double-pulse PIV is conducted in a seeded air jet at different velocities and seeding densities, evaluating the effects of latency on pulse separation, 2D particle image reconstruction, and subsequently the quality of cross-correlation. In both sets of experiments, a reference sCMOS PIV camera is used simultaneously for comparison. We identify the maximum event rate that the camera can sustain before the readout process starts to experience saturation due to bandwidth limitations. This represents an operational limit for event-based PIV, and provides important guidance for selecting experimental conditions to avoid data loss.

2.2 Experimental Methods

Figure 2.1 shows a schematic of the experimental setup, including a 532 nm pulsed Nd:YAG, CFR PIV-200 Big Sky laser (Quantel) operated at 10 Hz. A laser sheet was formed using a combination of cylindrical lenses and trimmed to a height of 60 mm with a slit to ensure

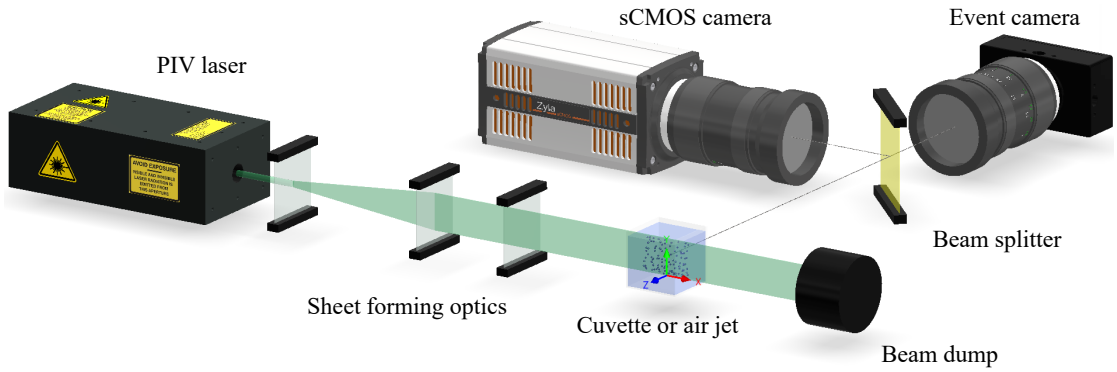

Figure 2.1 Experimental setup

relatively uniform illumination across the field of view (FOV). The thickness of the laser sheet was roughly 500 μm [63], and the relative standard deviation of the shot-to-shot laser energy was less than 3%.

A Prophesee EVK2 Gen 4.2 HD event camera, with the 1280 $\times$ 720 pixel Sony IMX636 sensor, was used, as in a recent EBIV study [39]. The camera has a manufacturer quoted maximum event rate of 1066 ev/μs and nominal latency near 200 μs. The Prophesee interface sdk v4.5.2 was used to set adjustable detector parameters such as the contrast threshold and record data, while data was extracted and post-processed in Python. A reference Andor Zyla 5.5 sCMOS frame-based camera (2560 $\times$ 2160 pixel resolution) simultaneously imaged the flow with a 50:50 beam splitter (Edmund Optics 24037). Both cameras were equipped with a 532$\pm$5 nm filter to minimize background noise. The details of the optical system are listed in Table 2.1. The event and sCMOS cameras were spatially registered and mapped using a La Vision 106-10 target, and the residual mismatch (only a few pixels) was determined and corrected. A flashing lamp was used to ensure the event camera could resolve the static target. For the characterization test, the projected spatial resolution was kept similar for both cameras to ensure a comparable number of photons reached each pixel, see Table 2.1. For the PIV measurements, lenses were chosen to maintain a roughly equivalent field of view, with the PIV results from the sCMOS camera serving as the reference true velocity field for uncertainty analysis.

2.2.1 Test conditions

A summary of test conditions is provided in Table 2.2. In the event-camera characterization test, a 42.5 $\times$ 45 $\times$ 45 mm^3 cuvette was filled with a suspension of water and 1-2 μm diameter alumina particles (Al_2O_3), a typical PIV tracer for both liquid and gaseous flows. Individual Mie scattering images with uniform particle distribution were obtained using single-pulse

Table 2.1 Configuration of the optical system

Camera	Experiment	Lens	f/D	Projected spatial resolution (μm/px)	Field of view (mm^2)
EVK2 Gen 4.2	Characterization test (water/alumina suspension in a cuvette)	Tokina 100 mm	8	21.61	27.7 × 15.6
	PIV measurements (air jet seeded with alumina particles)	Nikon 35 mm	8	60.42	77.3 × 43.5
Andor Zyla 5.5	Both experiments	Tokina 100 mm	8	27.17	69.6 × 58.7

laser illumination. Different seeding densities were achieved by adding dilution water to an initial densely seeded suspension. Before each Mie scattering image was acquired, the water was manually stirred, to avoid particle deposition on the inner walls of the cuvette, and allowed to settle for 30 seconds. The residual momentum in the cuvette resulted in a flow of roughly 2 mm/s during data collection. The entire FOV (27.7 × 15.6 mm^2) of the event camera was well withing the cuvette, away from all inner surfaces, such that no unwanted reflections were collected by the event camera.

To investigate the effects of laser energy, seeding density, and the preset contrast threshold (at which an event is triggered) on the output event rate (and the performance of the camera), tests were conducted with 9 different laser energies ranging from 0.4 mJ to 20.7 mJ (with corresponding laser fluences from 1.3 to 69 mJ/cm^2), 10 particle image densities ranging from 3.6×10^{-4} to 12.5 ppp (particles per pixel), and 7 contrast threshold values from 20% to 80%. Note that the same contrast threshold was set for both ON and OFF events for all test conditions. Unless the threshold was the changing variable, it was kept constant at 80% to suppress unwanted background noise, based on a reference configuration experiment (laser on, cuvette removed).

In the second set of experiments, PIV measurements with double-pulse illumination were conducted in a jet of air at different bulk flow velocities, particle seeding densities, and laser pulse intervals. For bulk velocities above 1 m/s, a converging nozzle with a 32 mm exit diameter was used to generate the air jet; for lower velocities, a 100 mm diameter tube was adopted to maintain a minimum flow through the seeder. Air was seeded with the same alumina particles as in the cuvette experiments. The recorded event data were extracted to reconstruct pairs of 2D Mie scattering "pseudo-images" as described in [37], and used to determine the velocity field of the flow in Davis 10.

Table 2.2 Summary of test conditions

Series	Parameter	Value / Range
Characterization test (water/alumina suspension in a cuvette)		
Baseline parameters		
E	laser energy (fluence)	14.4 mJ (48 mJ/cm^2)
S	particle image density	3.7×10^{-3} ppp
P	particle image size	2.6 px
C	contrast threshold	80%
Variable parameters		
E	laser energy (fluence)	0.4–20.7 mJ (1.3–69 mJ/cm^2)
S	particle image density	3.6×10^{-4} – 12.5 ppp
P	particle image size	1.6–8.6 px
C	contrast threshold	20–80%
PIV measurements (air jet seeded with alumina particles)		
V	velocity	0.2–5 m/s (Re= 1355–10667)
I	pulse interval	500–30 μs
J	particle image density	8×10^{-3} – 7×10^{-2} ppp
T	contrast threshold	40%

2.3 Event camera characterization test using a water/alumina suspension in a cuvette

In this section, the response of the event camera (EVK2 Gen 4.2) to single-pulse laser illumination, and its capability to record the particle image field are presented and discussed.

2.3.1 Response to pulsed laser illumination

Figure 2.2 shows a typical temporal distribution of events generated from Mie scattering of the flowing water/alumina suspension. Although the laser pulse lasts only 8 ns, the resulting positive events are distributed over a much longer period, roughly 400 μs. Negative events then follow and continue to steadily occur until the next laser pulse. We define two types of event rates in this work. The instantaneous event rate is computed by dividing the number of events in each time bin by the bin width (50 μs in this case), and is shown on the right y axis of Figure 2.2. The average event rate refers to the total number of events divided by the duration over which they are generated, referred to as latency (further discussed in Section 2.3.2). Throughout the paper, unless otherwise specified, the term "event rate" (e.g., Figure 2.4) refers to the average event rate. The distribution of events shown in Figure 2.2 is attributed to a relatively long response time of the event camera, which is a function of both the implicit latency of individual pixels and the latency induced by the row arbitrage (which causes a loss of timestamp) in the readout unit. Following an intense laser pulse illumination, the voltage in each pixel experiences a quick rise before slowly decaying (similar

to the behavior of a photo-diode with a long response time), such that OFF events continue to be generated much longer than ON events.

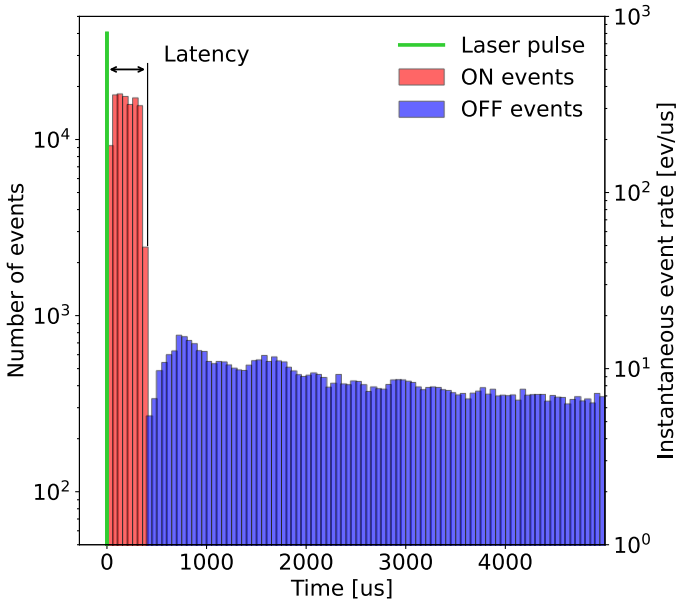

Figure 2.2 Temporal distribution of ON and OFF events following a 14.4 mJ laser pulse and particle image density of 2×10^{-2} ppp. The bin width is 50 μs

This "latency", which leads to a delay in event generation relative to the actual incident of the event, remains an active area of improvement within the neuromorphic imaging research community [37]. For pulsed PIV specifically, the latency directly affects the time window used to extract events associated with each laser pulse to reconstruct raw instantaneous Mie scattering pseudo-images, and subsequently the minimum pulse interval dt required to avoid the temporal overlap of events from two consecutive pulses. In PIV, the pulse interval is a key parameter that ensures the displacement of particles is neither too large (particles escape from the interrogation window) nor too small (large uncertainty) to effectively resolve the velocity and direction of the flow. The above implies that using event cameras to perform pulsed PIV adds complexity, requiring a meticulous balance among velocity dynamic range, magnification factor (spatial resolution), and the laser pulse interval.

As shown in Figure 2.2, OFF events have a long latency of a few milliseconds, making them impractical for PIV image reconstruction in turbulent flows which may have characteristic time scales of only a few hundred microseconds. Therefore, in the present work we only use and analyze ON events. Setting a higher threshold to OFF events than ON events can theoretically minimize the former (since they are not used) and save bandwidth for the latter, as suggested in [37, 39]. However, as shown in Figure 2.2, under the present setup,

ON and OFF events only overlap for roughly 2 μs, and are therefore unlikely to significantly affect the event camera's performance. To enable future comparison between pulsed PIV and continuously illuminated Lagrangian particle tracking [34], the same threshold was set for both ON and OFF events. We emphasize here again that throughout the rest of the paper, all the event histograms, event rates, recovered images, and analyses were performed using only ON events.

2.3.2 Latency

A latency of approximately 200 μs under pulsed illumination, as observed experimentally by [37] using an EVK2 (Gen 4.1 sensor), provides an estimate of the maximum sampling rate ($\sim$ 5 KHz). However, this latency is not a fixed value, as it varies with the input event rate. For EBIV with a pulsed laser, unlike for Lagrangian particle tracking (LPT) with an LED lamp or continuous wave laser, all laser-induced events are triggered within a few nanoseconds (the laser pulse width) during which the flow is assumed static. This implies that the event rate is decoupled from the velocity of the flow, and that the instantaneous input event rate after the pulse is extremely high, resulting on a significant "load" on the camera's sensor. While sensor load may be evaluated with the total number of events generated per laser pulse, in order to maintain consistency with previous studies on both EBIV and continuous illumination LPT (e.g. [25, 30, 39]), we used the average event rate as an indirect indicator to evaluate the load exerted on the camera for each test case.

Figure 2.3 shows the temporal distribution of event generation for three different cases, each with an increasing total number of events produced in response to a laser pulse. These variations were achieved by increasing either the laser energy (green bins) or the seeding density (gray bins) relative to a reference case (red bins). The latency is found to increase with the total number of events and the event rate, from 220 μs (reference case) to 310 μs and 380 μs for the green and gray cases respectively. Unsurprisingly, the more events triggered at the same time, the longer the waiting queue in the readout interface, and the longer it will take for all events to be read out. Note that, since the readout of events generated by the pixels is row-wise [12], the latency also varies row-wise, as further discussed in Section 2.4.3. The global latency is then defined as the time required for all ON events to be generated over the entire sensor area in response to a stimulus. Unless specified, the term "latency" in this paper denotes the "global latency".

Figure 2.4 summarizes the relation between latency and event rate by varying the laser pulse energy and seeding density in the water/alumina suspension (colored circles). Latency was calculated as the time when the instantaneous event rate (after smoothing with a window of 3 bins) drops below 1% of its maximum value, using a bin size of 1 μs. The latency

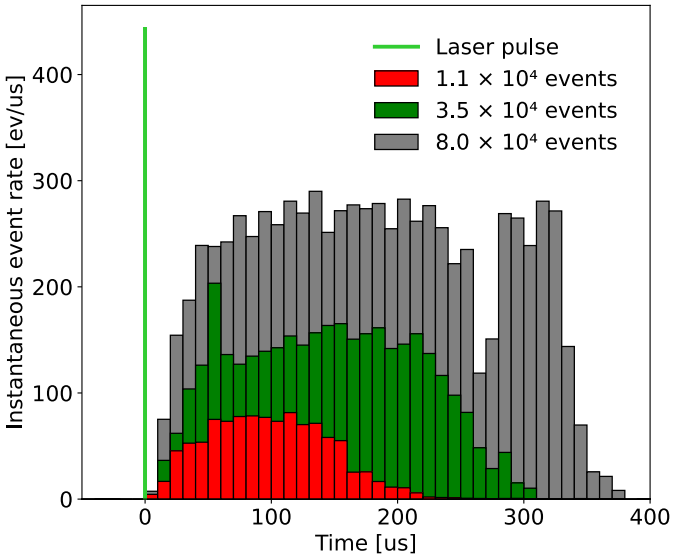

Figure 2.3 Temporal distribution of events generated in response to a laser pulse for reference case (red bins), and relative increases in laser energy (green bins) and seeding density (gray bins). The legend indicates the total number of ON events induced by the laser pulse. The instantaneous event rate is calculated based on a 50 μs bin size. Average event rates over the entire event distribution of the three cases are 50 ev/μs, 112.9 ev/μs and 210.5 ev/μs, respectively

increases as the event rate rises, reaching a maximum near 450 μs for an event rate of 400 ev/μs, after which it slightly decreases and eventually plateaus around 350 μs, possibly due to the sensor readout saturation. For event rates greater than 400 ev/μs, the sensor reaches its bandwidth limit and can no longer process all incoming data, causing some of the rows in the queue of the readout interface to be skipped or unrecorded, resulting in non-retrievable information loss. Since fewer rows are read out, the total readout time shortens, resulting in the observed decrease in latency. While this interpretation is consistent with the observed plateau in latency, further investigation would be required to confirm that sensor readout saturation is indeed the cause. A related analysis by Cao et al. [30], using a digital micro-mirror device to simulate particle motion, showed that the sampling frequency of the event camera converges to a value near 2400 Hz as the particle concentration increases. Although their analysis focuses on sampling rate rather than latency, this convergence can be interpreted as equivalent to the latency plateau observed here. In both cases, the sensor reaches a bandwidth limit where increasing the event load no longer results in increased temporal response, indicating the onset of readout saturation and potential data loss.

The performance curve shown in Figure 2.4 serves as an important tool for EBIV measurements, as the latency indicates the minimum pulse interval that can be used without data

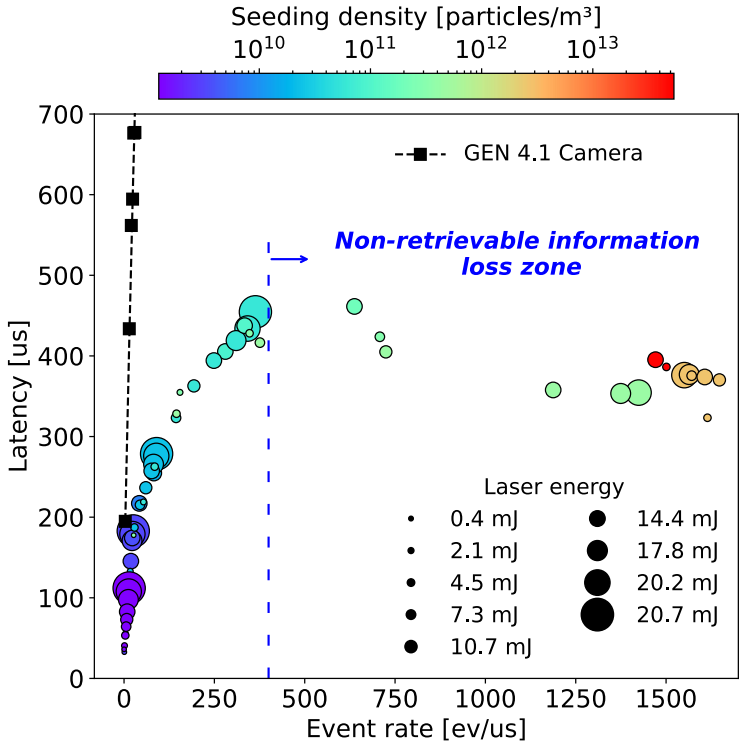

Figure 2.4 Latency distribution of the EVK2 Gen 4.2 as a function of event rate for data series E and S in the water/alumina suspension. The different marker sizes represent the 9 levels of laser energy in mJ/pulse, while the colors indicate seeding density in particles/m^3 (estimated based on the approach in [64] for a laser energy of 14.4 mJ/pulse). Black squares represent data points obtained using a previous generation EVK2 Gen 4.1 camera

loss, which directly determines the velocity dynamic range. For comparison, the performance curve of a previous generation Prophesee EVK2 camera (Gen 4.1 sensor) was determined using the same methodology. Results are plotted as black squares in Figure 2.4, showing the significantly longer latency of the Gen 4.1 sensor compared to the Sony IMX636 sensor in the Gen 4.2 at the same event rate, where non-retrievable information loss also starts at much lower event rates, near 30 ev/μs, as opposed to near 400 ev/μs. As new generations of event-based devices with higher bandwidth and shorter latency continue to emerge, the same approach can be readily used to assess their suitability for EBIV.

2.3.3 Information loss

Due to the latency of event cameras, events are accumulated over a defined time window to form a 2D pseudo-image, also referred to as "time correction" [37]. This consists of binning events, initially in 3D space (x, y, t), along the time t axis to reconstruct a 2D image. The time window used to bin the events and retrieve the 2D image is referred to as the accumulation

time (acc). This approach has been adopted throughout the literature [30, 44, 65, 66]. Unlike continuous illumination, in pulsed laser illumination, events will effectively represent the particle position during the (relatively short) laser pulse, despite the temporal latency of the camera.

To ensure the reconstructed 2D event pseudo-images effectively resolve the camera's entire field of view, the accumulation time should be equal to or greater than the latency, otherwise entire rows of data that are read out afterwards will be omitted, as shown in Figure 2.5 (a) and (b). The shorter the accumulation time relative to the latency, the more rows of data may be omitted from the reconstruction, observed from the left to right columns in the figure. For moderate particle image densities up to 2×10^{-2} ppp ($\sim$ 20 particles per 32 $\times$ 32 interrogation window) in (a) and (b), a full pseudo 2D image was consistently recovered by ensuring a sufficiently long accumulation to collect all the events. Hence, the potential information loss caused by an accumulation time that is too short, which leads to missing rows in the pseudo-image reconstruction, is considered retrievable. However, further increasing the particle image density to 4.5×10^{-2} ppp ($\sim$ 46 particles per 32 $\times$ 32 interrogation window), or even (1×10^{-1} ppp), as shown in Figure 2.5 (c) and (d), leads to information loss that is considered non-retrievable, regardless of accumulation time, as rows of event data are skipped/unrecorded due to readout saturation, as discussed above. It must be noted that most pixels either generated no event (blank) or one single event (red) after the laser pulse, yet on a few pixels up to 8 events can be stacked up over the accumulation time. This suggests a potential delayed response of the pixel to strong Mie scattering signals produced by the pulsed laser illumination, causing multiple events to be triggered at the same pixel, but at different timestamps. We hypothesize that this effect could explain why the non-retrievable information loss may only cause a "faded" row with less events, instead of an entirely empty row with zero events, as shown by the first column in Figure 2.5 (c)(d).

The camera's performance is presented in Figure 2.6 (a) and assessed by measuring the number of active rows on reconstructed pseudo-images at different accumulation times. To determine whether a row is active, a threshold was set at 60% of the average number of events per row for each condition. Rows falling below this threshold were considered to be either missing or skipped/unrecorded. This includes rows where information is only partially lost, as in the "faded" rows described above. For cases with very low seeding-densities ($<$ 3.7×10^{-3} ppp), a lower threshold of 10% was used to accommodate the inherent sparsity of particle images. The effectiveness of this approach was verified manually for each condition to ensure missing rows were effectively identified.

Figure 2.6(a) shows that for shorter accumulation times, rows of data are lost at lower event rates (black vs. orange markers). Note that the sensor has a total of 720 rows,

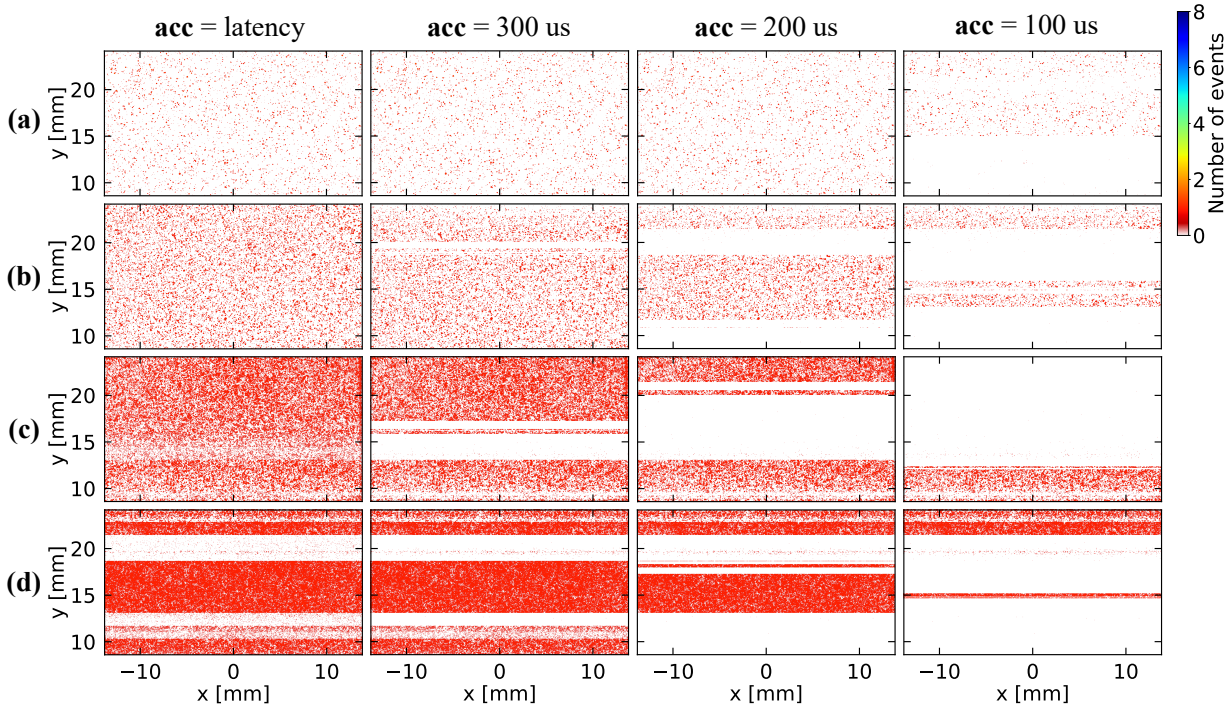

Figure 2.5 Reconstructed pseudo-images generated from four different seeding cases in the S data series, accumulated over various time intervals. Only ON events are presented. The laser energy was 14.4 mJ and the particle image densities a) 3.7×10^{-3}, b) 2.0×10^{-2}, c) 4.5×10^{-2}, and d) 1.0×10^{-1} ppp. The corresponding latency values were a) 255 μs, b) 405 μs, c) 461 μs, and d) 358 μs

corresponding to the maximum value on the y-axis. Beyond 400 ev/μs, the sensor bandwidth is exceeded, leading to non-retrievable information loss that becomes more significant at higher event rates. Figure 2.6(b) highlights the maximum event rate as a function of the minimum accumulation time needed to recover a full pseudo-image, defined as having 95% of the total rows being retrieved (the 5% margin incorporates a small uncertainty for low seeding cases where a few pixel rows may not contain any particles). The standard deviation of shot-to-shot fluctuation is plotted as error bars. The figure implicitly provides the shortest pulse interval (which is equivalent to the minimum accumulation time) needed to fully reconstruct the first frame in an EBIV image pair, as a function of event rate. This is a critical parameter to consider in order to ensure EBIV measurements are performed effectively. For instance, in the current experiments, event rates above 400 ev/μs inevitably resulted in missing rows. Having established the relationship between the event rate and the temporal latency, the effects of laser fluence, seeding density, particle image size, and contrast threshold on the camera's event rate will be discussed and quantified.

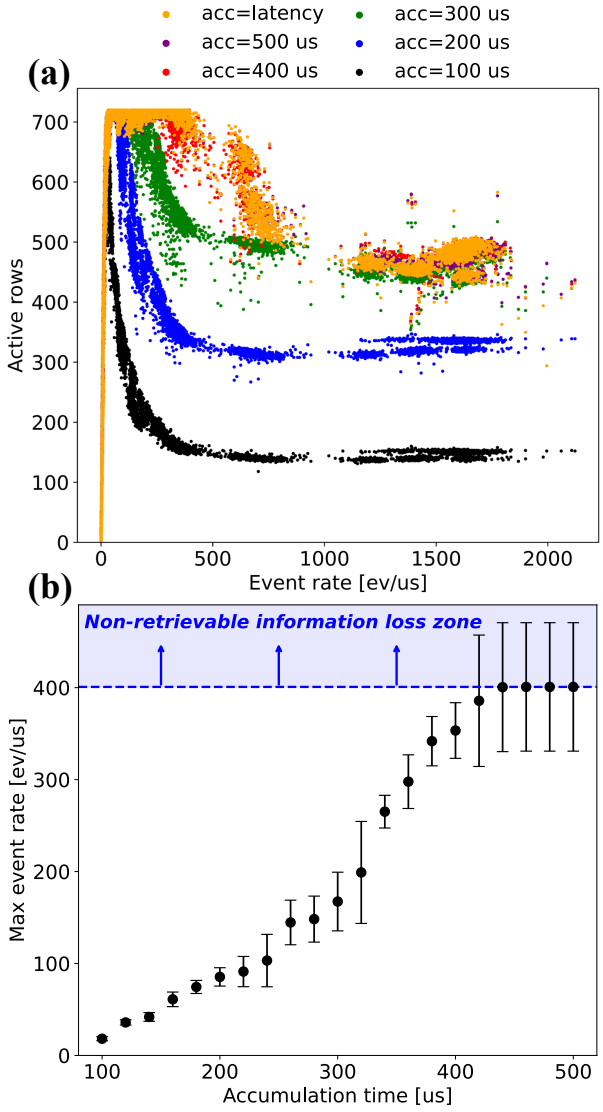

Figure 2.6 (a) Number of active rows at different tested event rates, post-processed using various accumulation times. Each dot represents a pseudo-image reconstructed from a single laser pulse. For each of the 61 tested conditions in data series E and S, 200 laser pulses were recorded and processed. *acc=latency* refers to an accumulation time long enough to capture all the events generated by the corresponding laser pulse, varying for each case; (b) Maximum event rate for each accumulation time that ensures that at least 95% of rows are captured in the pseudo-image reconstruction. The error bars represent the shot-to-shot standard deviation

2.3.4 Effect of laser pulse energy

In most applications of PIV, a relatively low laser pulse energy, on the order of a few millijoules at 532 or 527 nm is more than sufficient. The resulting Mie scattering from tracer particles 1-2 μm in diameter produces a signal strong enough for non-intensified sCMOS and Charge-

Coupled Device (CCD) cameras, while minimizing unwanted background scattering. Figure 2.7 shows a 5×5 mm region of interest (ROI) for the sCMOS camera (top row) and event camera (bottom row) at (a) 2.1, (b) 10.7, and (c) 20.7 mJ. To generate the pseudo-image, events were accumulated over the corresponding latency time of 133, 237, and 279 μs for (a), (b), and (c), respectively. The projected spatial resolution is kept similar between both cameras. A relatively high contrast threshold of 80% was used to ensure background noise was excluded.

It must be noted that in the sCMOS camera images, the colourscale represents the pixel count, while in the event camera pseudo-images, the colourscale represents the number of events registered at each pixel. This is an important distinction that serves as a reminder that the pseudo-images (as they are here processed) are not a grayscale representation of Mie scattering intensity as in the sCMOS images, but rather strictly indicate the location and frequency of events associated with seeding particles over a defined time window. For some of the larger particles, more than one event may occur at a single pixel, as discussed above, which occurs predominantly for the larger particles illuminated by the pulsed laser.

The pseudo-images therefore do not resolve the 2D Gaussian intensity distribution of individual particles as do the grayscale sCMOS images, shown in Figure 2.7. This can lead to peak locking, as observed by [39], and has implications for the processing and resulting uncertainty of PTV and PIV measurements, which will be further discussed in Section 2.4.2.

Comparing the sCMOS and event results, Figure 2.7 shows that the number of particles detected by the event camera is consistently lower than that of the sCMOS camera. In particular, it appears the weakest Mie signals in the sCMOS image, caused either by smaller particles or lower laser energy, were not captured by the event camera. To illustrate this, particles detected by the event camera are overlaid as red circles on the sCMOS image in Figure 2.7(a), top row. Several of the small/weak particles in the sCMOS image are missing from the event pseudo-image, confirming they were not detected by the event sensor. While lowering the contrast threshold of the event camera would effectively increase the number of detected particles, this would also introduce unwanted random noise, which cannot be distinguished and therefore separated from particle signals.

As expected, both cameras detect a greater number of particles as the laser energy increases. The particle image density (i.e. the number of particles per pixel, ppp) is plotted as a function of laser energy in Figure 2.8, with the corresponding event rates shown on the right y axis. To quantify ppp from the event data, an algorithm was developed that calculates the total number of particles in the field of view by detecting and grouping events occurring in adjacent pixels into distinct clusters, each representing a single particle. For the sCMOS camera, particles were identified using a corner detection algorithm [67], which searches for

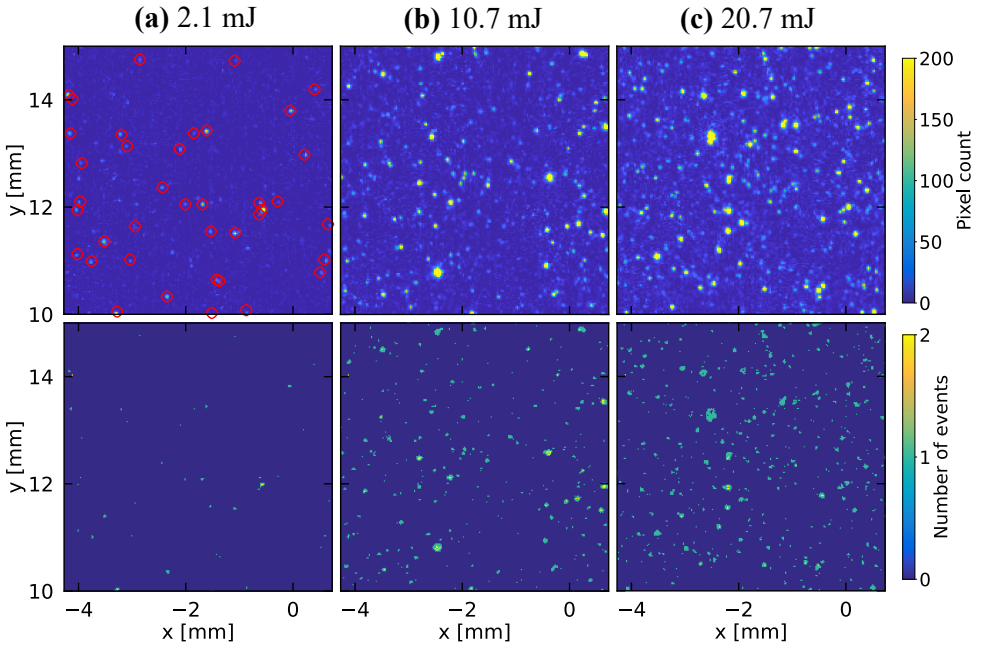

Figure 2.7 sCMOS images (top) and event pseudo-images (bottom) for three different laser energies and the same region of interest (ROI). In (a), red circles indicate the position of particles detected by the event camera, overlaid on the corresponding sCMOS image

areas with high intensity gradients caused by the peak intensity at the center of each particle. For both algorithms, several individual images were inspected manually to confirm that over 95% of the particles were detected, in order to enable a sound and quantitative comparison.

2.3.5 Particle image density

In PIV measurements, particle image density significantly affects the robustness of the cross-correlation and resulting velocity field. Sparse particle images may lead to missing and spurious vectors, and excessive seeding can lead to loss of correlation due to particle image overlap. It also influences the finest flow structures that can be resolved by enabling the selection of a smaller interrogation window and a shorter pulse interval. In particular, for measurements in flames, the seeding density drops by a factor of $\sim$ 7 downstream of the flame front due to thermal expansion from ambient temperature reactants below 300 K to products over 2000 K. A sufficiently high seeding rate is therefore needed to resolve the flow field through the flame. Selecting particle seeding density correctly can significantly improve the measurement accuracy and completeness of the velocity field.

The effect of particle image density on the output event rate of the EVK2 IMX 636 is shown in Figure 2.9. For low to moderate seeding cases (a) and (b) up to 3.7×10^{-3} ppp, particle image

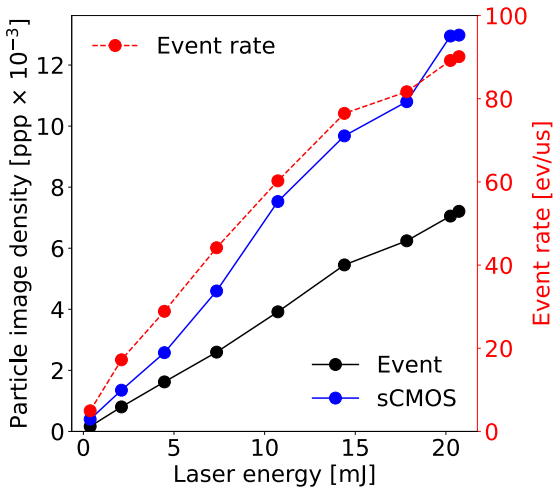

Figure 2.8 Particle image density (left y-axis) for sCMOS and event camera, and event rate (right y-axis) as a function of laser energy for the E data series. Each point on the graph represents the mean value calculated from 200 images for a fixed seeding density

density was determined using the particle detection algorithm described in Section 2.3.4. For higher seeding density cases (c), (d), and (e), the algorithm underestimates the particle image density as particle clusters and skipped/unrecorded rows (due to readout saturation) are observed in the event pseudo-images. The particle image density is thus extrapolated from the low-seeding cases, based either on the proportionality of the dilution of the water/alumina suspension, or on the proportionality of the average intensity in the same region of interest (ROI) recorded by the sCMOS camera. Both approaches yield similar estimates over the seeding density range tested.

In Figure 2.9, the blue dashed line indicates where non-retrievable information loss starts ($\sim$ 400 ev/μs), included for reference. We also observed that the event rate increases near-monotonically before plateauing at particle densities above 0.1 ppp due to readout saturation. As the water/alumina suspension in the cuvette flows at a velocity of only a few millimeters per second, the velocity field can be obtained by times-series PIV operating at 10 Hz. The relationship among particle image density, event rate, and the resulting velocity field can therefore be evaluated without considering the effect of latency, as the pulse interval of 0.1 s is far longer than the camera latency. We plot the PIV result on Figure 2.9 for representative S cases. For reference, the recommended ranges of particle image density for PTV, PIV, and speckle PIV are highlighted above the figure following the definitions of [2, 15]. The gradient across the PIV colourbar represents the transition between the theoretical lower limit for particle image density and the practically recommended lower limit, which is 5–10 times greater. Note that there is an overlap between PTV and PIV, which is attributed to

high-density tracking approaches, e.g. [40].

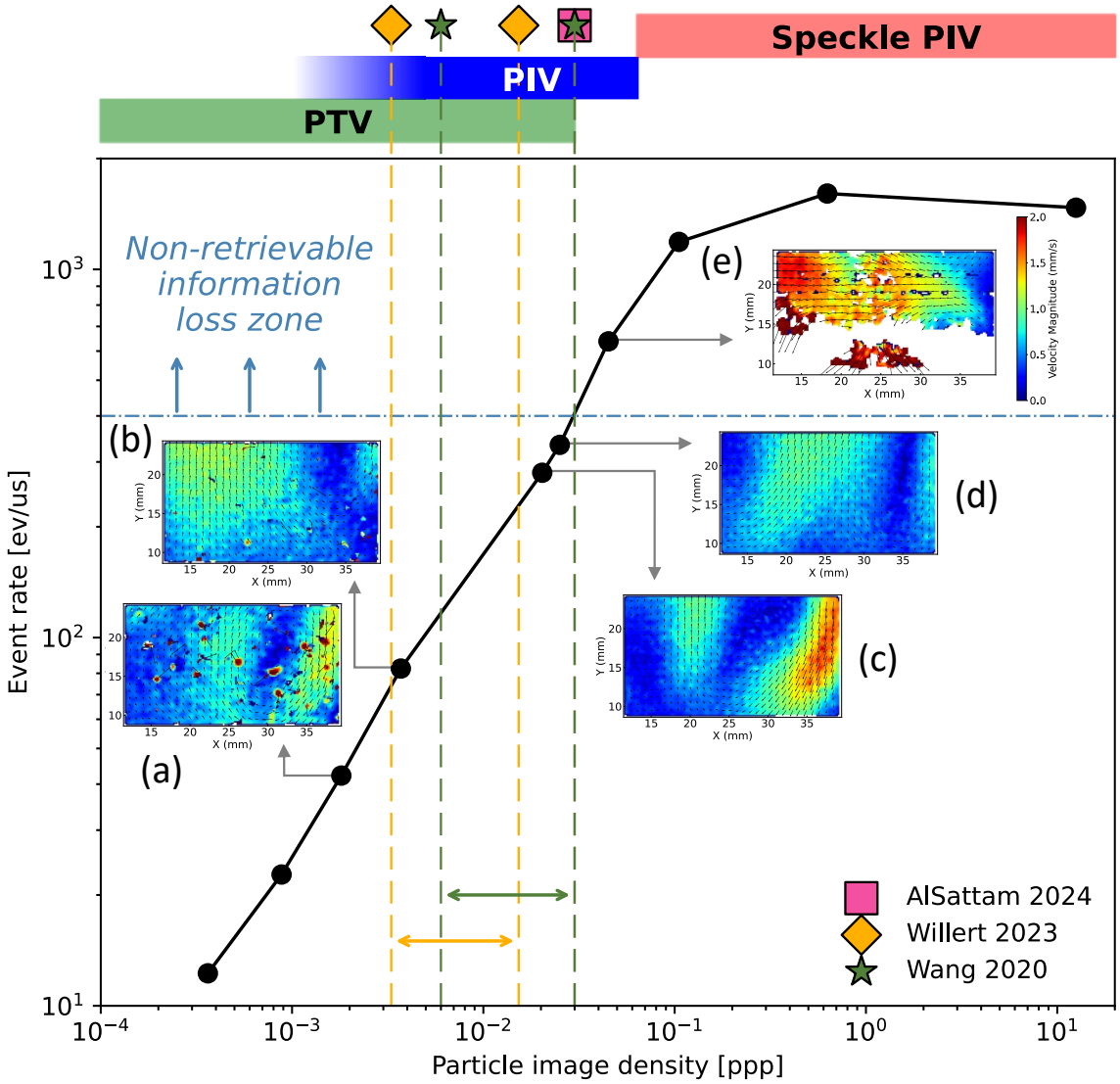

Figure 2.9 Event rate as a function of particle image density for S-series data, collected at 14.4 mJ laser energy. Particle image densities for PTV, PIV, and speckle PIV are based on those reported in [2, 15]. Subfigures (a)–(e) show representative EBIV velocity fields calculated from event pseudo-images at different seeding densities

For a low seeding density, although the event camera is not saturated, overly sparse seeding leads to spurious vectors, as shown by the vector field for case (a) 2×10^{-3} ppp. Reliable PIV images were observed for case (b) 3.7×10^{-3} ppp, with the most promising results for cases (c) 2×10^{-2} ppp and (d) 2.5×10^{-2} ppp. These results and the defined PIV range agree with the particle image densities used in [37] to obtain exploitable EBIV results, which are included in the figure. At higher particle image densities above 3×10^{-2} ppp, the event

camera begins to experience readout saturation, leading to skipped/unrecorded rows and incomplete velocity fields, as illustrated in case (e). These results suggest that for the low velocities of the water/alumina suspension, where the pulse interval of 0.1 s is significantly longer than the camera latency, particle image densities ranging from $\sim$ 0.0037-0.03 ppp enable robust PIV measurements. We also highlight the particle image densities applied by previous event-based particle tracking studies on Figure 2.9, including [34] and [40], which all fall within the defined PTV window. This particle image density range ($\sim$ 4-30 particles per 32 $\times$ 32 px window) is sufficient to ensure a robust and complete velocity field for EBIV, with very few spurious or missing vectors. The upper limit also provides a strong margin to accommodate strong gradients in effective seeding density in the flow, such as in combustion applications mentioned above. At lower particle image densities, where the accuracy of EBIV measurements is compromised due to an insufficient number of particles, event-based particle tracking is a viable alternative, analogous to the relationship between PIV and PTV.

2.3.6 Particle image size

Given the relevance of defocusing PIV, astigmatic PTV, tomographic PIV, and PIV in macroscopic flows to the flow velocimetry community [68], we also include an analysis of the effect of particle image size on the event pseudo-images. Ten levels of defocus (P-series data) were evaluated by gradually adjusting the camera position along the z-axis, i.e., the normal distance to the laser sheet. Figure 2.10 illustrates the appearance of particle images at three different levels of defocus. As the camera comes out of focus, the particles appear larger and more diffuse, while the laser energy and seeding density were held constant. We quantified particle size by calculating an equivalent diameter using the number of active pixels forming each particle as the area, which ranged from 1.6 to 8.6 pixels across the evaluated cases. As shown in Figure 2.11, when the camera is out of focus, the light intensity decreases, resulting in fewer particles being detected. However, the number of events generated by each particle increases due to their larger apparent size.

To evaluate the behavior of event generation under different defocusing, laser energy, and seeding conditions, the number of events per particle is plotted in Figure 2.12 for data series E, S, and P. A dataset featuring larger particle aggregates collected at various laser fluences is also included (triangles), obtained by not stirring the water/alumina suspense as thoroughly during preparation. The group of squares enclosed in the red oval on the top left of the figure represents the defocused cases (up to a 4.5 px diameter). It can be observed that, under the current optical configuration, fully focused particle images remain diffraction-limited, as most low to moderate seeding cases exhibit a relatively constant rate of 3-4 events per particle, even in the case of aggregates at low laser energies. For defocused particle images,

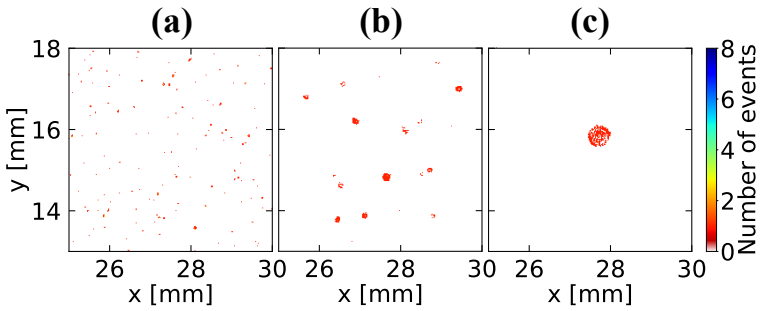

Figure 2.10 Event pseudo-images of the water/alumina suspension for three increasing levels of defocus, with equivalent particle image diameters of 1.6, 4.5, and 8.6 pixels, respectively. The fully focused reference pseudo-image in (a) corresponds to a particle image density of 2.2×10^{-3} ppp, compared to 1.8×10^{-4} in (b) and 9×10^{-6} ppp in (c)

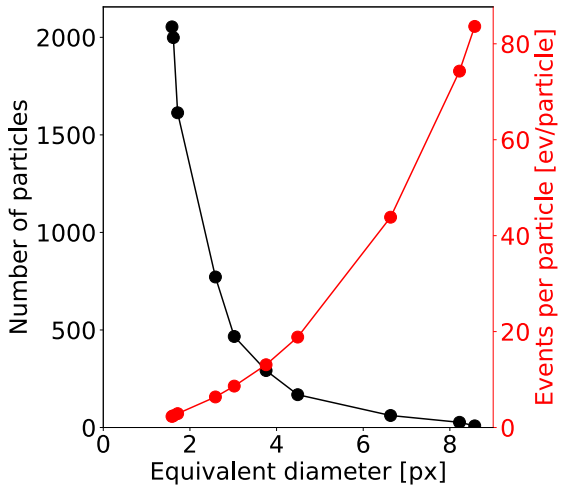

Figure 2.11 Number of particles and events per particle for various equivalent particle sizes at different defocusing levels. The seeding density and laser energy were held constant at 3.8 $\times$ 10^9 particle/m^3 and 14.4 mJ, respectively

the overall event rate remains relatively constant, while the number of events per particle increases significantly with the degree of defocus. At high seeding densities and high laser energies (indicated by larger red or orange markers), particle images begin to cluster, causing the particle identification algorithm to overestimate the number of events per particle.

Knowledge of the number of events per particle may be used to quickly estimate the maximum applicable particle image density. For instance, as shown in Figures 2.4 and 2.6(b), the maximum event rate before sensor saturation for the current EVK2 camera is approximately 400 ev/μs. Considering a latency of $\sim$400 μs and an average of 4 events per particle, this corresponds to a total number of roughly 40k particles on the 1280 $\times$ 720 px sensor (0.04

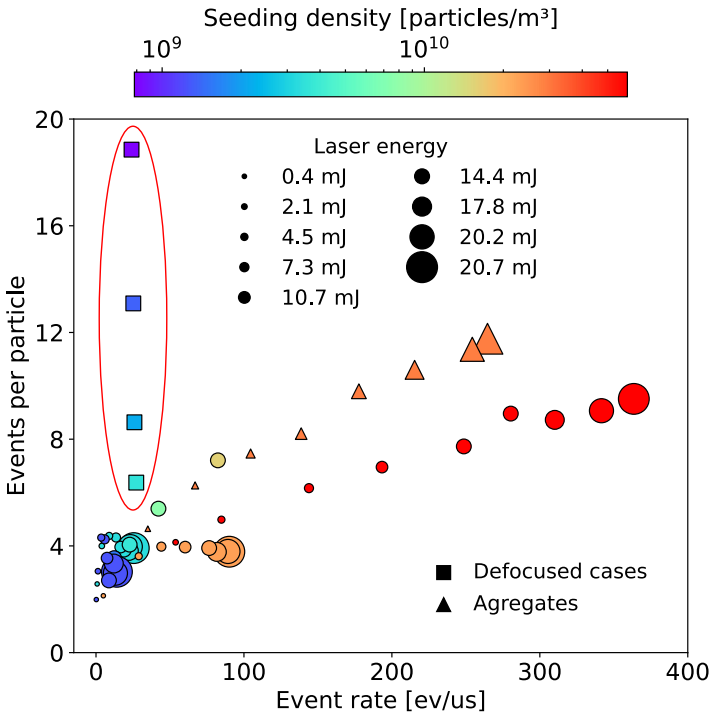

Figure 2.12 Number of events per particle for data series E, S, and P for event rates below the maximum of 400 ev/μs, such that non-retrievable information loss is not observed. Triangle markers represent an additional test case with particle aggregates, while square markers correspond to defocused conditions used to intentionally produce larger particle image sizes. The color bar indicates the seeding density in particles/m^3, quantified at a laser energy of 14.4 mJ

ppp). This estimate closely matches the previously identified threshold of 0.03 ppp at which sensor saturation effects begin to appear, as observed in Figure 2.9.

2.3.7 Effect of contrast threshold

In addition to the parameters associated with a conventional PIV setup, the user defined contrast threshold for event cameras introduces an additional tuning parameter in EBIV. For a laser power of 14.4 mJ and moderate particle seeding density of 3.8×10^9 particle/m^3, seven values of contrast threshold were tested, with the results shown in Figure 2.13. As expected, increasing the contrast threshold led to fewer particles being detected. This occurs because, at higher thresholds, the Mie scattering signal from smaller particles is no longer strong enough to reach the sensor's detection limit (or threshold) and trigger an event. Consequently, fewer events are generated and the measured particle image density decreases. Adjusting the contrast threshold effectively balances event detection with latency reduction, and is often more practical than fine-tuning the seeding density, particularly when accurate

measurements are required at specific velocities.

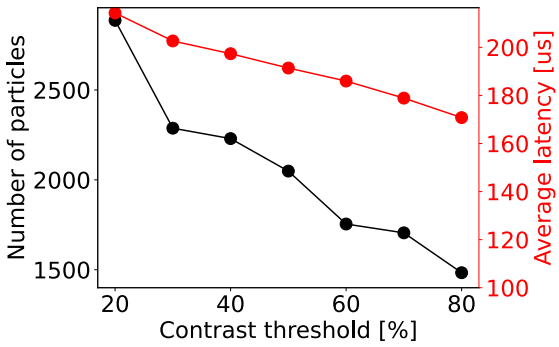

Figure 2.13 Impact of varying the contrast threshold (C data series) on the number of detected particles and latency in the event camera

2.4 Event-based PIV measurements in a seeded air jet

In the previous section, characterization experiments using a water/alumina suspension showed that for ultra low velocities on the order of 0.002 m/s, the delay between laser pulses of 0.1 seconds was consistently greater than the event camera's maximum latency. The accumulation time was therefore long enough to ensure event pseudo-images were fully reconstructed, effectively resolving the velocity field. In this case, the upper limit of particle image density is therefore constrained primarily by sensor saturation to avoid skipped/unrecorded rows.
For higher velocities, however, the analysis becomes more complicated, as the event camera's latency directly sets the minimum allowable time interval between the first and second PIV laser pulse, effectively defining the maximum measurable velocity. To evaluate the velocity dynamic range, PIV was conducted with both the event and sCMOS cameras in a seeded air jet for velocities ranging from 0.2 to 5 m/s. Events related to the first pulse were accumulated over the pulse interval dt, while those following the second pulse were accumulated for as long as required to ensure all events were captured. The interrogation window size was 32 $\times$ 32 px with 50% overlap for both the event and sCMOS data. The cameras were spatially registered and the velocity field obtained from the sCMOS served as the reference value when determining measurement error of EBIV.
Figure 2.14 shows the temporal event distribution under double-pulse illumination, the corresponding Mie scattering pseudo-image pairs, and a comparison between the instantaneous velocity fields obtained from the event and sCMOS cameras. It is important to note that the event camera was rotated 90° (relative to the cuvette experiments) to keep the longer dimension of the sensor aligned with the axial direction of the jet. The saturation of band-

width and non-retrievable information loss therefore appears as missing columns, instead of rows. Previous discussion on "row-wise" behavior will now be "column-wise".
For the higher velocity cases (d,e,f) tested with the 32 mm converging nozzle, the air jet did not fully occupy the camera's sensor, leaving some regions empty. This is due to the entrainment of non-seeded ambient air or the swaying of the low-velocity jet. Nevertheless, the jet consistently covered more than 95% of the sensor columns. In addition, only 1000 of the 1280 pixel rows along the axial direction were used due to the height of the laser sheet. This region of the sensor is not shown in the figures. We consider this level of coverage sufficient to justify using the water cuvette results (which cover the entire sensor) as a reference for interpreting the air jet measurements. For experiments in which the ROI represents a smaller portion of the sensor, it is suggested that the characterization test, as presented in Section 2.3, be performed using the same ROI.

2.4.1 Velocity dynamic range

Figure 2.14 (a) 0.2 m/s and (b) 0.5 m/s show the lowest bulk velocity cases, where the maximum observed velocities within the analysis ROI were roughly 0.5 and 1.0 m/s, equivalent to 8.3×10^{-3} and 1.7×10^{-2} px/μs, respectively based on the projected spatial resolution of the event camera. In both cases the laser pulse interval is greater than or equal to the event camera's maximum latency of $\sim$ 400 μs. As a result, the events corresponding to each laser pulse are well separated and therefore easily allocated to their respective pseudo-image. Intriguingly, the event distributions further show that roughly twice as many events follow the second laser pulse than the first, despite similar pulse energies. It is hypothesized that this is due to residual voltage accumulated at pixels that did not reach the contrast threshold with the first laser pulse, and did not fully decay before the second pulse. When the second laser pulse occurs, this residual voltage combined with the new intensity increase easily exceeded the contrast threshold, thereby triggering events. This slow decay may also help explain the long latency of OFF events observed in Figure 2.2. Nevertheless, both event pseudo-images are fully recovered, with the resulting EBIV vector field showing excellent agreement with that of sCMOS PIV. Results were consistent for most of the 200 instantaneous flow realizations, except for a few with lower particle image densities due to variations in seeding density. In this configuration, for flows requiring laser pulse intervals greater than the camera latency, particle image densities up to 0.06 ppp can be used with the EVK2, before non-retrievable information loss occurs. For the current air jet experiment, this corresponds to $\sim$ 500 ev/μs which is a slightly higher value than the quantified limit of 400 ev/μs from the cuvette in Figure 2.9, likely due to the slightly smaller active area of the sensor mentioned above, which caused a fewer number of events in each column.

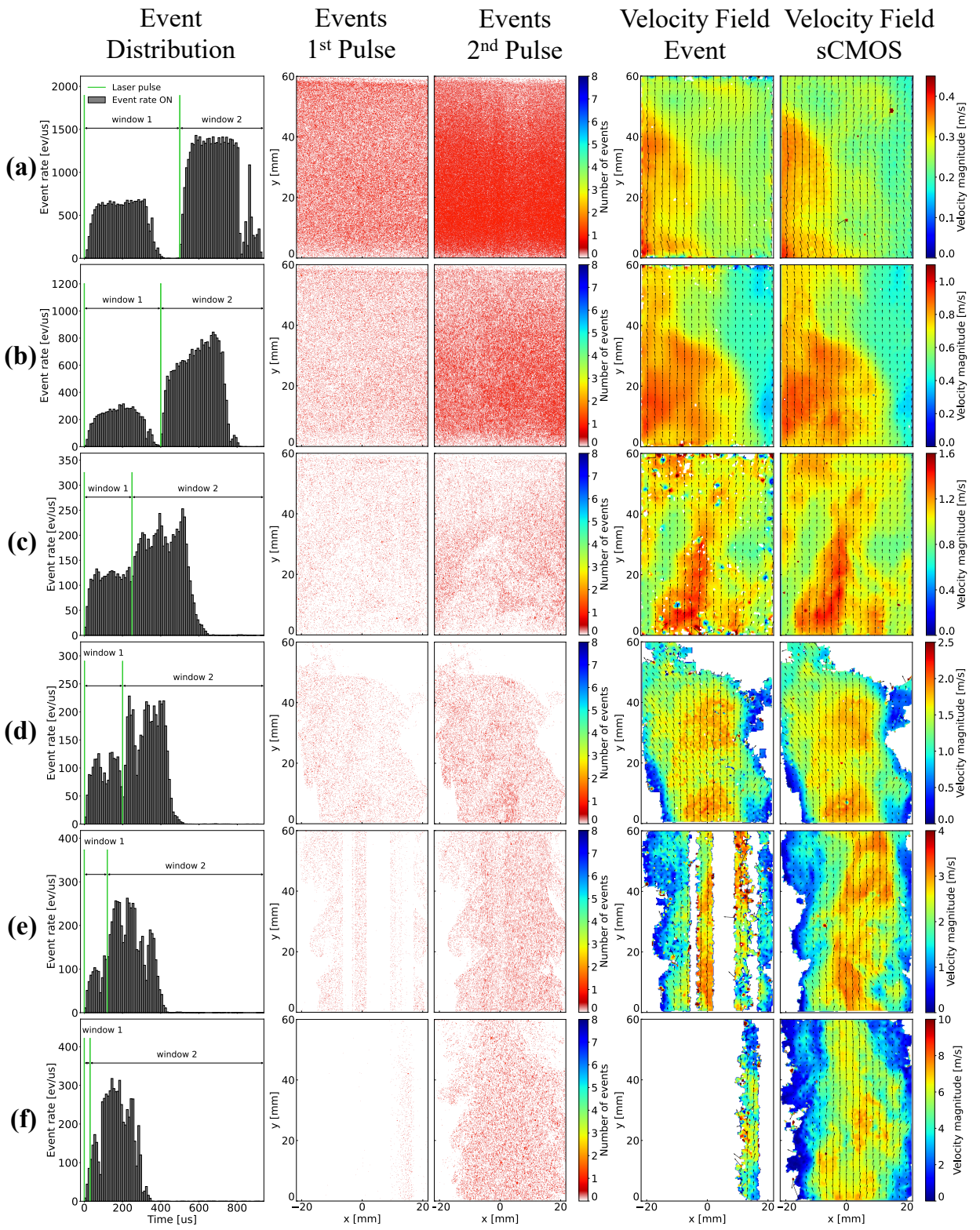

Figure 2.14 Event distribution following first and second PIV laser pulses, corresponding Mie scattering event pseudo-images, and resulting vector fields for air jets with bulk velocities 0.2, 0.5, 0.8, 1.2, 2, and 5 m/s (Re = 1355, 3387, 5419 for D = 100 mm, and 2560, 4267, 10667 for D = 32 mm, respectively). The pulse intervals were set to 500, 400, 250, 200, 120, and 30 μs, respectively, ensuring that particle displacements in high-velocity regions of the flow remained within 3–7 pixels. For both the event and sCMOS cameras, particle displacements typically fell within one quarter of the interrogation window size. The laser pulse energy was approximately 14.4 mJ

As the bulk flow velocity increases to 0.8 m/s (maximum velocity of 1.5 m/s, equivalent to 2.5×10^{-2} px/μs), the laser pulse interval approaches or even falls below the latency of the first frame, causing some events from the first pulse to be read out in the same time window as events from the second pulse. This subsequently weakens the cross-correlation, as some events associated to the first pulse are captured in the second frame (or pseudo-image), and leads to a larger uncertainty in EBIV. As shown in Figure 2.14(c), spurious vectors begin to appear, and the resulting velocity field becomes more noisy.

The quality of the event based results was also affected by inconsistencies in seeding density during the air jet experiments. Unlike the cuvette where the seeding density remains stable and is easy to adjust, the seeding in the air jet varies throughout the test. For the 1.2 m/s case (maximum velocity 1.8 m/s, equivalent to 3×10^{-2} px/μs), as the pulse interval approaches 200 μs, the range of event rates that both avoids saturation and provides sufficient particle image density narrows, as observed in Figure 2.6(b). Consequently, due to both variations in seeding density and an extremely narrow window on the applicable particle image density, fewer than 5% of the recorded images yielded a complete velocity field. While a complete velocity field is shown in Figure 2.14(d), in most instantaneous vector fields, columns were missing.

As the bulk velocity increases to 2 and 5 m/s in (e) and (f) (maximum velocity 3 and 7 m/s, equivalent to 5×10^{-2} and 1.2×10^{-1} px/μs), the pulse intervals dt are set to 120 and 30 μs, respectively. This further reduces the accumulation time of the first PIV frame (window 1), and increases the number of events from the first laser pulse that continue to be readout after the second laser pulse, during the accumulation time for the second PIV frame (window 2). At these velocities, a very low event rate would be necessary to ensure a camera latency shorter than time delay between laser pulses, such that the particle image density would be too sparse to allow for exploitable PIV measurements.

For these higher velocity flows, event-based PTV may be an interesting alternative to EBIV, at a low particle image density which can be derived from Figure 2.6(b) and Figure 2.9. For instance, if a pulse interval of 30 μs is needed, where the maximum event rate is ~ 6.2 ev/μs, this corresponds to a particle image density of roughly 5×10^{-5} ppp, i.e., approximately 46 particles for the full field of view (assuming a mean of 4 events/particle based on the results in Figure 2.12).

To clearly illustrate the correct selection of particle image density based on the maximum event rate, the 1.2 m/s bulk velocity case was repeated at different particle image density levels using a pulse interval of 200 μs. Six representative instantaneous vector fields from these tests are shown in Figure 2.15 (a-e). These six vector fields are also plotted on the maximum event rate vs. accumulation time plot obtained from the water cuvette measurements in

Figure 2.6 (b), which is reproduced. Of the six cases, only (b) and (c) result in a complete and sound velocity field, with no missing columns and only a few spurious vectors. Note that (b) and (c) fall roughly within the error bars of the water cuvette characterization. Below this range, (a) falls within the event rate range but has an overly sparse particle image field that yields a large amount of spurious vectors, whereas (d-f) show a number of empty columns as they far exceed the optimal event rate range. This indicates that a particle image density of 0.018 ppp, as in case (b), represents the lower limit to obtain a reliable velocity field using EBIV. This value falls within the acceptable range defined in Figure 2.9.

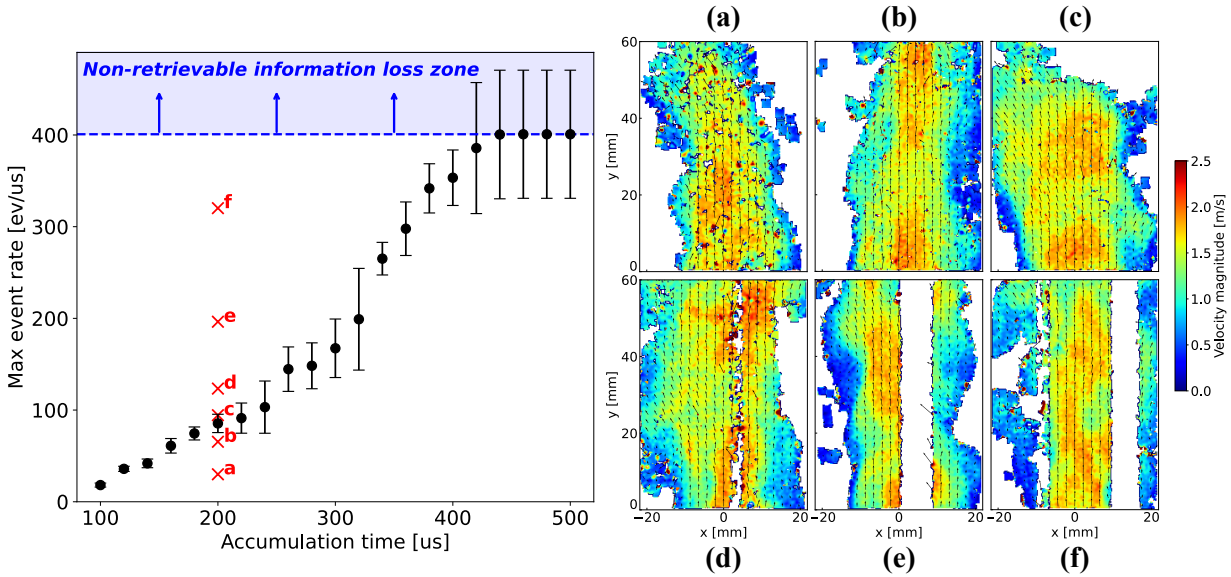

Figure 2.15 Six example instantaneous vector fields from the 1.2 m/s air jet, plotted onto Figure 2.6 at a pulse interval of 200 μs. The corresponding event rates and particle image densities are: (a) 30.0 ev/μs - 9.7×10^{-3} ppp, (b) 65.4 ev/μs - 18.5×10^{-3} ppp, (c) 94.4 ev/μs - 2.7×10^{-2} ppp, (d) 123.4 ev/μs - 3.4×10^{-2} ppp, (e) 196.3 ev/μs - 5.0×10^{-2} ppp and (f) 320.2 ev/μs - 6.5×10^{-2} ppp

With the above analyses, for the present setup, the maximum velocity that can be measured is roughly 1.8 m/s (0.03 px/μs). The lowest velocity tested in the present study is 0.2 m/s (3.3×10^{-3} px/μs) in the air jet and 2 mm/s (9.3×10^{-5} px/μs) in the water cuvette, and can theoretically be even lower, until Brownian motion of particles starts to affect the measurements [2]. Willert [37], who also used a pulsed laser and the previous generation of the same camera (Gen 4.1 HD), demonstrated EBIV in a velocity range of 1.5 m/s (0.04 px/μs) to 3 m/s (0.14 px/μs), which changes depending on the experimental setup, projected spatial resolution, and region of interest. Similarly, Willert and Klinner [62] reported a maximum reliable velocity of 1.5 m/s (0.03 px/μs), aligning well with the present analyses.

2.4.2 Uncertainty analysis

The uncertainty of the PIV results was determined using LaVision 10, which follows the methodology described in [69, 70]. As previously noted, event pseudo-images do not resolve the Gaussian intensity distribution of particles, such that the residual displacement for each particle has an inherent error of up to 0.5 pixels due to peak-locking. Assuming a normal distribution within the ±0.5 pixel range (where $\sim \pm 0.5\,\text{px}$ corresponds to $\pm 3\sigma$), the rms of the residual displacement (the rms error) is expected to have a baseline value of 0.16 px.
To compare the EBIV results with those of sCMOS PIV, the Root Mean Square Error (RMSE) between the instantaneous velocity fields obtained with both techniques was calculated. Since the two cameras have different spatial resolutions, the RMSE was computed using a normalization factor α that converts velocity magnitudes into displacements in pixels. The RMSE is given by:

$$\text{RMSE} = \sqrt{\frac{\sum_{i=1}^{N}(\alpha_{\text{EVENT}} V^i_{\text{EVENT}} - \alpha_{\text{sCMOS}} V^i_{\text{sCMOS}})^2}{N}}, \tag{2.2}$$

where V^i is the local velocity magnitude at interrogation window i, and N is the number of interrogation windows. The calculation was performed within a selected region of interest where events were recorded, excluding empty columns resulting from saturation. The normalization factor α is defined as:

$$\alpha = \frac{\Delta t}{r}, \tag{2.3}$$

where Δt is the pulse interval in μs (200 μs in this case), and r is the spatial resolution of the camera in μm/px, as reported in Table 2.1 for the air jet experiments.
Figure 2.16 (a) illustrates the uncertainty of EBIV for a velocity of 1.2 m/s (equivalent to 2×10^{-2} px/μs), for event rates ranging from 0 to 1750 ev/μs. The pulse interval was kept constant at 200 μs. It can be clearly seen that the uncertainty decreases rapidly as the event rate increases from 0 to 50 ev/μs. This is attributed to the rise in particle image density, which significantly improves the cross-correlation by mitigating the effects of overly sparse seeding. However, beyond 220 ev/μs, the uncertainty gradually increases as the latency approaches the laser pulse interval, causing some events generated by the first pulse to be read out during the time window assigned to the second pulse, which weakens the cross-correlation. Figure 2.16 (b) plots RMSE with event rate, showing a similar trend to (a). Notably, the high RSME for event rates below 50 ev/μs is attributed to a large uncertainty in both EBIV and sCMOS PIV, because the overly sparse particle image density affects both measurements.
To better illustrate the trade-off between uncertainty and the completeness of the velocity

field, both the uncertainty and the number of missing columns within the 0–220 ev/μs range are plotted in Figure 2.16 (c), together with the RMSE in (d). The 1 m/s case was selected because the jet was formed using a 100 mm tube, which provided relatively stable seeding and full event coverage across the entire field of view (see Figure 2.14 (a) to (c)). As a result, the camera's response to varying event rates in this configuration is more consistent (with less scatter in the number of missing columns). However, further increasing the event rate is limited by the capacity of the seeder. Similar to Figure 2.16 (a), an initial drop in the uncertainty is observed in the 0-50 ev/μs range, before quickly stabilizing at $\sim$ 0.37 px. In parallel, the number of missing columns increases near 80 ev/μs, due to an accumulation time (200 μs) that is shorter than the camera latency, which aligns with that predicted in Figure 2.6 (b). The RMSE also drops from 2.5 px to 0.3 px as the event rate increases from 10 to 200 ev/μs, shown in (d). To keep the RMSE below 1 pixel, a minimum particle image density of 0.015 ppp was required, consistent with the defined range for the water/alumina suspension in the cuvette in Figure 2.9.

2.4.3 Column-wise latency and adaptive accumulation time

The analyses throughout the paper have thus far been based on the reconstruction of pseudo-frames using a global accumulation time for the entire sensor. As the readout is column-wise (or row-wise in the water cuvette experiment), a local accumulation time specific to each column may be used to avoid missing columns, i.e., using an adaptive accumulation time. In this section, the feasibility to perform adaptive column-wise accumulation is investigated.
To further highlight column-wise readout, two example event pseudo-image pairs are presented in Figure 2.17 for a bulk flow velocity of 1.2 m/s. The event rate in both cases was $\sim$ 200 ev/μs, at which non-retrievable information loss (due to readout saturation) is very unlikely ($>$ 400 ev/μs), such that missing columns in the reconstructed pseudo-images were solely caused by the accumulation time being shorter than the camera latency. The first two columns in Figure 2.17 show the pseudo-images of the first and second frames using global accumulation times for all columns. The colormap represents the timestamp at which each column was read out, highlighting the lose of asynchronicity due to the camera's latency. The histogram in the third column plots the local event distribution extracted from three regions of interest (a, b, and ref), each corresponding to a 5 column-wide band. In the reference band (ref), which does not exhibit missing columns, a cluster of two bins is observed near 110 μs, and falls within the global accumulation window. Events from the first and second laser pulse are therefore clearly distinguishable and allocated to the first and second frames, respectively. In contrast, this was not the case for regions a and b, where entire columns of the first frame were empty, as no events from the first pulse were captured using the same

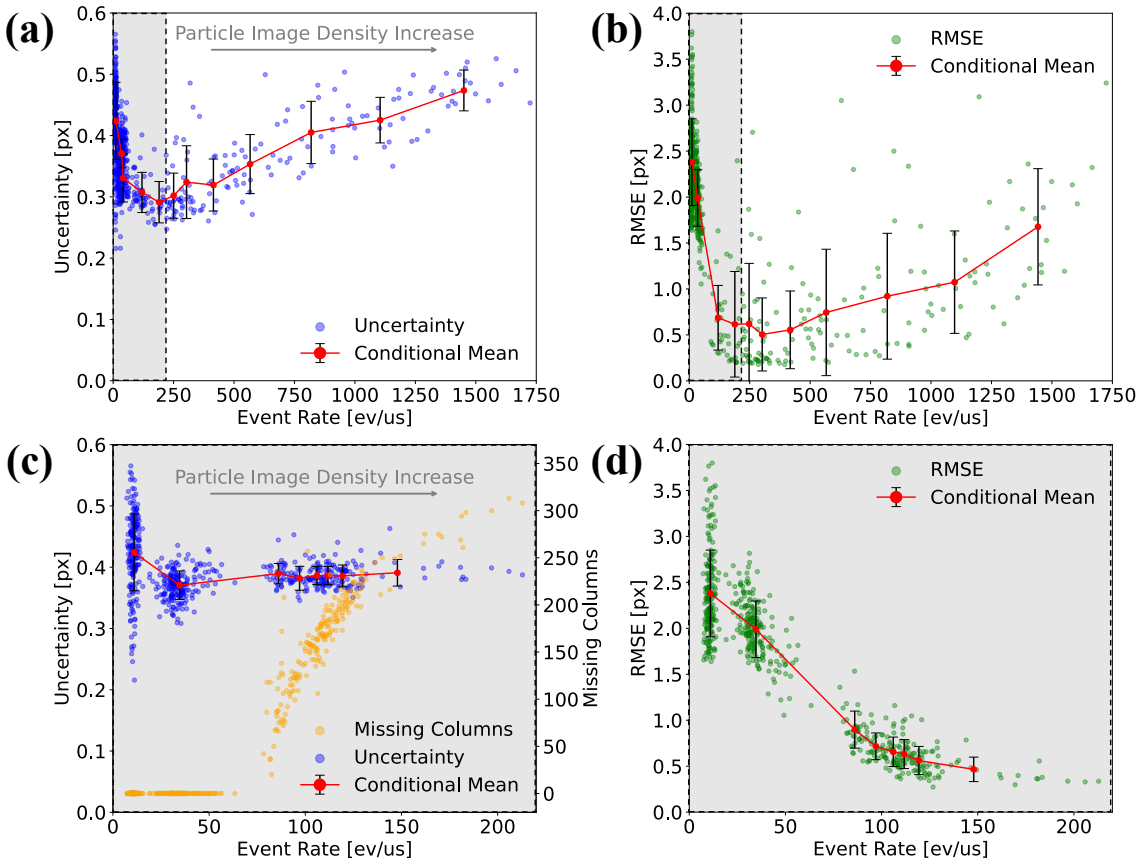

Figure 2.16 Uncertainty of the event camera and RMSE between the event camera and sCMOS camera. In (a) and (b) at 1.2 m/s with the 32 mm converging nozzle, and (c) and (d) at 1 m/s with the 100 mm tube. The shaded gray area in (a) and (b) highlights the region evaluated in (c) and (d) for comparison. Each point in the plot represents a single velocity vector field. The pulse interval was fixed at 200 μs

global accumulation time, because the corresponding bins (shown as blue and red near 200 μs in the event distribution histogram) lie outside the accumulation window. To address this, an adaptive accumulation time approach was attempted, with the results shown in the last two columns of Figure 2.17. The accumulation times for the missing regions were carefully adjusted based on their local event distribution, from the default 200 μs to 270 μs in (a) and 220 μs in (b), with the resulting pseudo-images shown in columns 4 and 5 of Figure 2.17. For both (a) and (b), the reconstructed first frames (column 4) show that previously empty columns are now populated. However, in (a), the second frame (column 5) now contains fewer events in the same region, indicating that events resulting from the second laser pulse are now accumulated on the first frame. This is also clearly illustrated in the event distribution diagram, where the prominent red bin near 240 μs contains events from both pulses. To further investigate this, the accumulation time was gradually increased in 1 μs increments,

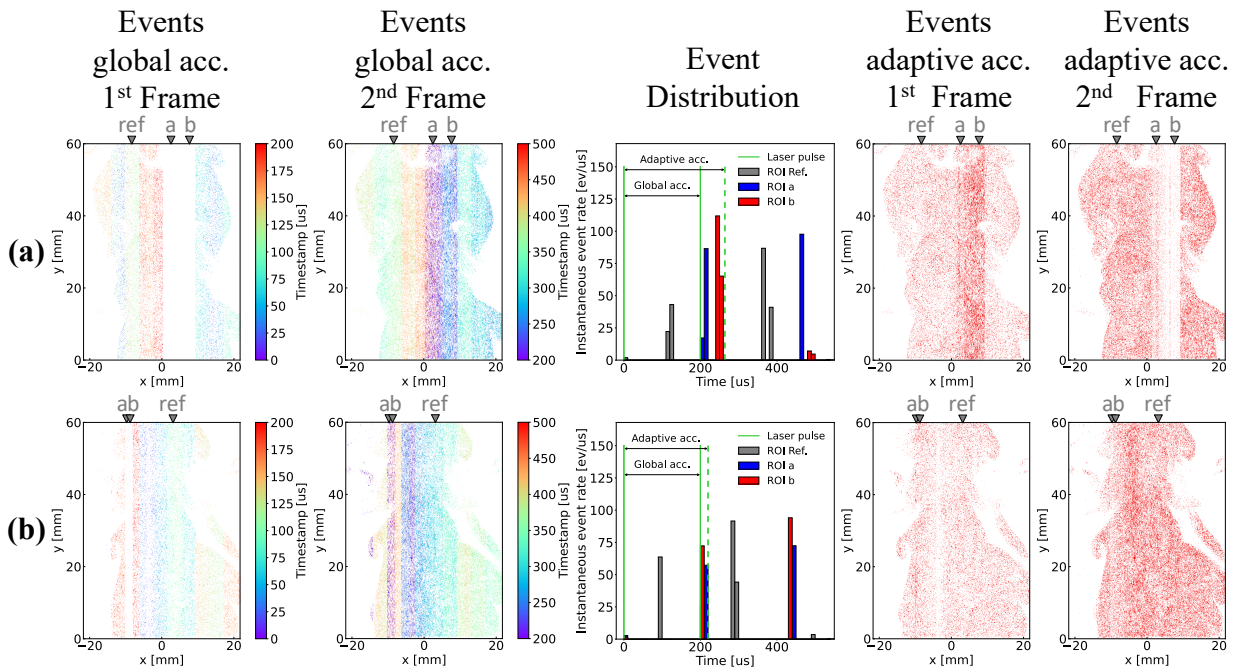

Figure 2.17 Example EBIV pseudo-images in (a) and (b) investigating the feasibility of adaptive event accumulation. Column 1-2: the first and second frames are reconstructed using a global accumulation time (equal to the laser pulse interval 200 μs). Regions a and b indicate missing column bands, while ref marks a reference region with no missing columns. The colormap shows the timestamp at which each column was read out. Column 3: local event distributions (bin size = 10 μs) extracted from each 5-column-wide band (a, b, and ref). Column 4-5: reconstructed first and second frames using adaptive accumulation. The event rate in (a) and (b) was $\sim$ 200 ev/μs, non-retrievable information loss was not observed

and it was observed that, at certain pixel columns, a significant amount of events associated with the first and second laser pulses were read out together during the same 1 μs time window. This implies that for these columns, many of the events from both laser pulses cannot be distinguished temporally, as they have the same time-stamp. This was less evident in (b), as suggested by the event distribution histogram, which showed clearly distinguishable groups of bins for each laser pulse. Adaptive accumulation was therefore more effective, as both frames were successfully recovered with events more evenly distributed across the field of view, shown in columns 4 and 5.

The corresponding velocity fields from event-based global/adaptive accumulations are compared to a reference velocity field obtained using the sCMOS camera in Figure 2.18. While both test cases show better agreement with the sCMOS when using adaptive accumulation, in particular (b), the velocity field in (a) remains incomplete with spurious vectors between lateral positions x = 0-9 mm. Although this issue could be mitigated by adjusting the delay

between laser pulses and/or the event rate (with a lower seeding/particle image density), this can lead to greater measurement uncertainty. Other methods, beyond the scope of the present work, may therefore need to be explored to identify which events correspond to the first and second laser pulses and reassign them to their respective pseudo-image. For instance Willert [71] recently proposed an imaging approach that overcomes sensor latency by using two event cameras (both equipped with the same IMX 636 sensor as used in the present study), with laser pulses that are orthogonally polarized. This approach effectively decouples the two event streams, allowing for much shorter pulse intervals, down to 1 μs, and enabling reliable velocity measurements at flow speeds up to 180 m/s.

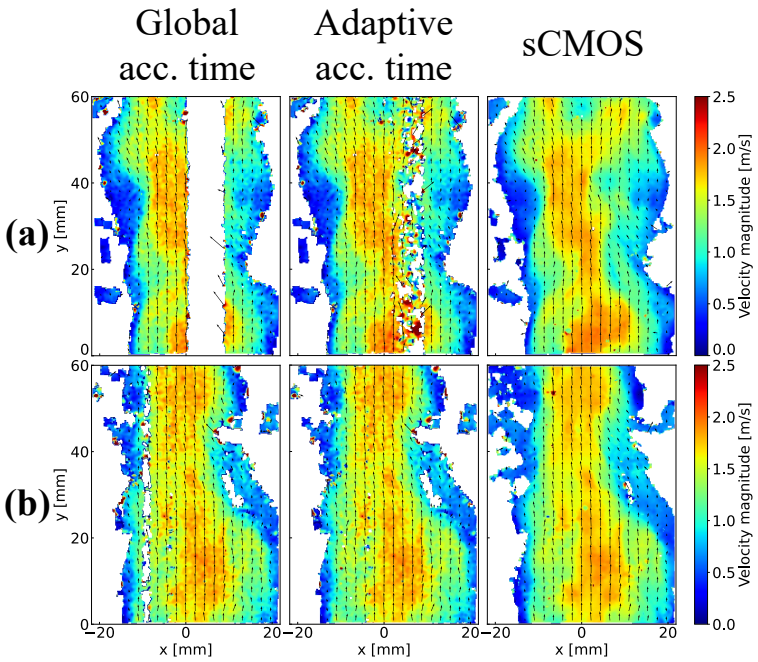

Figure 2.18 Event-based velocity fields obtained using global and adaptive accumulation times compared to a reference sCMOS camera for test cases (a) and (b) from Figure 2.17

2.5 Conclusion

In this work, we developed and demonstrated an experimental methodology to characterize the measurement capabilities of event cameras for PIV applications with pulsed illumination. Characterization experiments using a water/alumina particle suspension flowing in a cuvette were conducted to first asses the event camera's response to a single laser pulse. It was found that the event camera's latency does not remain constant and is affected by the number of events instantly and simultaneously generated by laser illumination. Additionally, non-retrievable information loss was observed row-wise due to saturation in the readout interface,

appearing at event rates above 400 events/μs. A performance map was established for the Prophesee EVK2 event camera in Figure 2.6(b), based on which users may determine the maximum event rate (without saturation) in order to set an accumulation time suitable for applying PIV to the desired velocity measurements. Performance maps can also be produced for other event cameras following the same methodology.

Key variables including laser energy, particle image density, particle image size, and contrast threshold were further investigated to explore their effects on the event rate. The applicable range of particle image density for PIV and PTV was defined based on values reported in the literature. Results suggested that for EBIV, particle image densities between 0.0037-0.03 ppp ensured a robust velocity measurement without skipped/unrecorded rows/columns or spurious vectors. Additionally, adjusting the contrast threshold proved to be an effective way of controlling particle detection, offering a practical alternative to physically changing the seeding density.

Double pulsed EBIV was then conducted in an air jet seeded with the same alumina particles used in the cuvette to quantify the velocity dynamic range. The trade-off among the laser pulse interval (velocity dynamic range), particle image density, and robustness of the velocity field was investigated at various jet velocities and seeding densities. A reliable PIV velocity field was obtained with particle image densities from 0.018 ppp which leads to a maximum measurable velocity of roughly 0.03 px/μs (equivalent to 1.8 m/s in the current setup) with a measurement uncertainty of 0.3 px.

It was further observed that, although events are generated at individual pixels independently and asynchronously following laser illumination, the readout interface processes them row/column-wise, causing pixel asynchronicity to be lost. This becomes more significant when many events are being generated in a short time. When the delay between laser pulses is shorter than the camera's latency, a non-negligible amount of events from the first and second laser pulses are read out together and assigned identical timestamps. As a result, these events cannot be separated and allocated to their corresponding pseudo-image solely based on the timestamp, since they appear indistinguishable in time, despite originating from different laser pulses. This issue therefore cannot be fully resolved using the proposed adaptive accumulation time approach, indicating that other methods may need to be further explored, such as the two-camera imaging solution demonstrated by Willert [71].

Although EBIV has yet to achieve the velocity dynamic range and measurement uncertainty of conventional PIV with frame-based sCMOS or CCD cameras, the low cost, flexibility, and significantly reduced data stream of event cameras make them a promising option worth further investigation for flow visualization. With the rapid development of event-based technology with higher data bandwidth and shorter latency, the proposed methodology could

contribute to establishing standardized calibration procedures and practical guidelines for EBIV using next generation cameras.

Acknowledgements

The authors are grateful for the technical support of Yin Yang of the NRC and Philippe Versailles of Polytechnique Montréal.

Declarations

- Funding: Financial support for this research was provided by the NRC's Aerospace Strategic Client Services program, the NRC's New Beginnings Initiative, the Natural Sciences and Engineering Research Council of Canada (RGPIN-2019-04309, RGPAS-2019-00131), and Environment and Climate Change Canada.

- Conflict of interest: The authors have no relevant financial or non-financial interests to disclose.
- Ethics approval and consent to participate: Not applicable
- Consent for publication: All authors consent to the publication of this manuscript in the Experiments in Fluids journal.
- Data availability: Data supporting the results of this study can be provided by the authors upon request.

CHAPTER 3 CONCLUSION

The objective of this research was to develop a methodology to characterize how latency and bandwidth limitations in event cameras affect the velocity dynamic range in event-based velocimetry, specifically pulsed Particle Image Velocimetry (PIV).

3.1 Summary of Works

The work presented in Chapter 2 addressed the objectives outlined in Section 1.6.2 by conducting a series of experiments and analyses, as described below:

A pulsed PIV experiment was conducted using a water cuvette seeded with particles and illuminated by a laser sheet. This setup allowed to characterize the latency and bandwidth limitations of the event camera, two key constraints previously identified in the literature as limiting factors for event-based velocimetry. By systematically varying the event rate, the latency behavior of the sensor could be identified. These findings are essential for determining the velocity measurement range, as latency directly limits the temporal resolution, specifically, the minimum time interval between laser pulses in a PIV measurement.

Using the same setup, the influence of key PIV parameters was investigated, including laser energy and particle image density, as well as user-defined event camera settings such as the contrast threshold, all of which affect event generation. To validate the results and benchmark the event camera's performance, comparative measurements were conducted using a conventional PIV frame-based camera.

As a result, a performance map summarizing the sensor's velocity measurement limits in terms of accumulation time, which is the minimum allowable time between pulses, was produced. This accumulation time is directly related to the camera's latency. For each of the tested accumulation times, the maximum permissible event rate before significant information loss occurred due to bandwidth saturation was determined. In addition, PIV velocity fields were computed for various seeding densities, allowing to define a suitable particle image density range for reliable event-based PIV measurements, supported by findings reported in the literature.

To demonstrate the applicability of the results obtained in the water cuvette, PIV experiments were conducted using a seeded air jet, following the pulsed-EBIV methodology proposed by Willert [37]. The measurements were compared against those of a conventional Andor Zyla 5.5 PIV camera. Several flow velocities and pulse intervals were tested, and the seeding density was also varied. The quality of the resulting velocity fields was consistent with the produced performance map previously established in the water-based experiments for each

pulse interval. The maximum measurable velocity under the tested conditions was 0.03 px/us (1.8 m/s).

These results confirm that event cameras are a viable and cost-effective alternative for fluid velocimetry. However, their current operational limits still constrain their use in high-speed flows and high-resolution PIV applications. Despite these limitations, event camera technology is evolving rapidly, with newer sensors offering increasingly improved specifications. In this context, the proposed characterization methodology becomes essential for evaluating the suitability of emerging event cameras for PIV applications.

3.2 Limitations

The proposed methodology for characterizing latency and bandwidth for PIV is easy to replicate for any event camera, requiring only a basic pulsed PIV experimental setup. However, the specific results presented in this study are not generalizable to all event cameras and are specific to the Sony IMX636 sensor. As event camera technology is evolving rapidly, with frequent updates in specifications, any new sensor should be independently characterized using the same methodology to ensure accurate performance assessment.

Due to the nature of the readout process in event cameras, the number of active pixels significantly influences the maximum event rate that can be sustained without data loss. In this study, the characterization was performed using the full sensor field of view. If a significantly smaller region of interest (ROI) is used, the bandwidth behavior may change, and the characterization should be repeated under those specific conditions.

3.3 Future Research

Future studies could explore the use of continuous-wave (CW) laser illumination to evaluate how event cameras perform under different lighting conditions in velocimetry. This would provide a broader understanding of how latency and bandwidth constraints influence performance in CW configurations, and whether the high temporal resolution of event cameras can be used more effectively under such conditions.

In the PIV experiments conducted in this thesis, when the event rate exceeded the defined maximum usable value for the used pulse interval, but remained below the non-retrievable information loss threshold (400 events/μs), some events from the first pulse were not fully processed in time and leaked into the second pulse. Separating these events based on their timestamps was attempted, but they were read out at the exact same microsecond and could not be distinguished temporally. A promising direction for future research would be to explore methods for separating overlapping events spatio-temporally. This could significantly

improve the usable velocity range and expand the potential of event-based velocimetry.

REFERENCES

[1] R. Goldstein, Ed., *Fluid Mechanics Measurements*. Taylor Francis, 1996. [Online]. Available: https://www.taylorfrancis.com/books/edit/10.1201/9780203755723/fluid-mechanics-measurements-goldstein

[2] R. J. Adrian and J. Westerweel, *Particle image velocimetry*. Cambridge university press, 2011. [Online]. Available: https://www.cambridge.org/ca/universitypress/subjects/engineering/thermal-fluids-engineering/particle-image-velocimetry?format=HB&isbn=9780521440080

[3] M. Raffel *et al.*, *Particle image velocimetry: a practical guide*. springer, 2018. [Online]. Available: https://link.springer.com/book/10.1007/978-3-319-68852-7

[4] M. Versluis, "High-speed imaging in fluids," *Experiments in fluids*, vol. 54, pp. 1–35, 2013.

[5] C. Mead, "Analog vlsi and neutral systems," *NASA STI/recon technical report A*, vol. 90, p. 16574, 1989. [Online]. Available: https://ui.adsabs.harvard.edu/abs/1989STIA...9016574M/abstract

[6] M. Maher *et al.*, "Implementing neural architectures using analog vlsi circuits," *IEEE Transactions on Circuits and Systems*, vol. 36, no. 5, pp. 643–652, 1989.

[7] C. Mead, "Neuromorphic electronic systems," *Proceedings of the IEEE*, vol. 78, no. 10, pp. 1629–1636, 1990.

[8] M. A. Mahowald and C. Mead, "The silicon retina," *Scientific American*, vol. 264, no. 5, pp. 76–82, 1991.

[9] P. Lichtsteiner, C. Posch, and T. Delbruck, "A 128 $\times$ 128 120 db 15 μs latency asynchronous temporal contrast vision sensor," *IEEE Journal of Solid-State Circuits*, vol. 43, no. 2, pp. 566–576, 2008.

[10] C. Posch, D. Matolin, and R. Wohlgenannt, "A qvga 143 db dynamic range frame-free pwm image sensor with lossless pixel-level video compression and time-domain cds," *IEEE Journal of Solid-State Circuits*, vol. 46, no. 1, pp. 259–275, 2011.

[11] C. Brandli *et al.*, "A 240 $\times$ 180 130 db 3 µs latency global shutter spatiotemporal vision sensor," *IEEE Journal of Solid-State Circuits*, vol. 49, no. 10, pp. 2333–2341, 2014.

[12] T. Finateu *et al.*, "5.10 a 1280×720 back-illuminated stacked temporal contrast event-based vision sensor with 4.86 µm pixels, 1.066 geps readout, programmable event-rate controller and compressive data-formatting pipeline," in *2020 IEEE International Solid-State Circuits Conference - (ISSCC)*, 2020, pp. 112–114.

[13] T. Lei *et al.*, "Motion measurements of explosive shock waves based on an event camera," *Optics Express*, vol. 32, no. 9, pp. 15 390–15 409, 2024.

[14] F. B. Insights, "Event camera market size, share covid-19 impact analysis," 2023. [Online]. Available: https://www.fortunebusinessinsights.com/event-camera-market-110552

[15] R. J. Adrian *et al.*, "Particle-imaging techniques for experimental fluid mechanics," *Annual review of fluid mechanics*, vol. 23, no. 1, pp. 261–304, 1991. [Online]. Available: https://www.academia.edu/download/73332358/fb3231b36d942b6ff1dacb8df68a6df9c9b0.pdf

[16] P. Buchhave, "Particle image velocimetry—status and trends," *Experimental Thermal and Fluid Science*, vol. 5, no. 5, pp. 586–604, 1992.

[17] J. Westerweel, G. E. Elsinga, and R. J. Adrian, "Particle image velocimetry for complex and turbulent flows," *Annual Review of Fluid Mechanics*, vol. 45, no. 1, pp. 409–436, 2013.

[18] LaVision, "Particle Image Velocimetry Techniques," 2025. [Online]. Available: https://www.lavision.de/en/techniques/piv-ptv/

[19] T. Dracos, "Particle tracking velocimetry (ptv)," in *Three-Dimensional Velocity and Vorticity Measuring and Image Analysis Techniques: Lecture Notes from the Short Course held in Zürich, Switzerland, 3–6 September 1996*, T. Dracos, Ed. Dordrecht: Springer Netherlands, 1996, pp. 155–160. [Online]. Available: https://doi.org/10.1007/978-94-015-8727-3_7

[20] M. Vollmer and K.-P. Möllmann, "High speed and slow motion: the technology of modern high speed cameras," *Physics Education*, vol. 46, no. 2, p. 191, 2011.

[21] T. Stoffregen, "Comparison of the data produced by an event camera and a conventional camera," August 14 2020. [Online]. Available: https://commons.wikimedia.org/wiki/File:Event_camera_comparison.jpg

[22] L. Steffen *et al.*, "Neuromorphic stereo vision: A survey of bio-inspired sensors and algorithms," *Frontiers in neurorobotics*, vol. 13, p. 28, 2019.

[23] T. Yoda *et al.*, "The dynamic photometric stereo method using a multi-tap cmos image sensor," *Sensors*, vol. 18, no. 3, p. 786, 2018.

[24] C. Posch *et al.*, "Retinomorphic event-based vision sensors: Bioinspired cameras with spiking output," *Proceedings of the IEEE*, vol. 102, no. 10, pp. 1470–1484, 2014.

[25] C. E. Willert and J. Klinner, "Event-based imaging velocimetry: an assessment of event-based cameras for the measurement of fluid flows," *Experiments in Fluids*, vol. 63, no. 6, p. 101, 2022.

[26] C. Scheerlinck, "How to see with an event camera," Presentation, Australian National University, Canberra, ACT, February 20 2020. [Online]. Available: https://www.cedricscheerlinck.com/talks/

[27] A. Vanarse, A. Osseiran, and A. Rassau, "A review of current neuromorphic approaches for vision, auditory, and olfactory sensors," *Frontiers in neuroscience*, vol. 10, p. 115, 2016.

[28] G. Gallego *et al.*, "Event-based vision: A survey," *IEEE Transactions on Pattern Analysis and Machine Intelligence*, vol. 44, no. 1, pp. 154–180, 2022.

[29] B. Chakravarthi *et al.*, "Recent event camera innovations: A survey," pp. 342–376, 2025.

[30] J. Cao *et al.*, "Benchmark evaluation of event-based imaging velocimetry using digital micro-mirror device," *Experiments in Fluids*, vol. 66, no. 4, p. 73, 2025.

[31] D. Drazen *et al.*, "Toward real-time particle tracking using an event-based dynamic vision sensor," *Experiments in Fluids*, vol. 51, pp. 1465–1469, 2011.

[32] J. Howell *et al.*, "High-speed particle detection and tracking in microfluidic devices using event-based sensing," *Lab on a Chip*, vol. 20, no. 16, pp. 3024–3035, 2020.

[33] D. Borer, T. Delbruck, and T. Rösgen, "Three-dimensional particle tracking velocimetry using dynamic vision sensors," *Experiments in Fluids*, vol. 58, pp. 1–7, 2017.

[34] Y. Wang, R. Idoughi, and W. Heidrich, "Stereo event-based particle tracking velocimetry for 3d fluid flow reconstruction," in *Computer Vision – ECCV 2020*, A. Vedaldi *et al.*, Eds. Cham: Springer International Publishing, 2020, pp. 36–53.

[35] A. Rusch and T. Rösgen, "Trackaer: real-time event-based quantitative flow visualization," *Experiments in Fluids*, vol. 64, no. 8, p. 136, 2023.

[36] C. E. Willert and J. Klinner, "Dynamic wall shear stress measurement using event-based 3d particle tracking," *Experiments in Fluids*, vol. 66, no. 2, p. 32, 2025.

[37] C. E. Willert, "Event-based imaging velocimetry using pulsed illumination," *Experiments in Fluids*, vol. 64, no. 5, p. 98, 2023.

[38] M. Raffel *et al.*, "Feasibility study of in-line particle image velocimetry," *Experiments in Fluids*, vol. 65, no. 3, p. 35, 2024.

[39] L. Franceschelli *et al.*, "An assessment of event-based imaging velocimetry for efficient estimation of low-dimensional coordinates in turbulent flows," *Experimental Thermal and Fluid Science*, vol. 164, p. 111425, 2025.

[40] O. A. AlSattam *et al.*, "Toward event-based noise-robust high density particle velocimetry," in *AIAA SCITECH 2024 Forum*, 2024, p. 2663.

[41] O. AlSattam *et al.*, "Kf-pev: a causal kalman filter-based particle event velocimetry," *Experiments in Fluids*, vol. 65, no. 9, p. 141, 2024.

[42] X. Zeng *et al.*, "A temporally adaptive particle tracking velocimetry using continuous-wave illumination for fused event- and frame-based cameras," *Journal of Visualization*, vol. 28, no. 3, pp. 463–486, 2025.

[43] Prophesee, "Sensor readout saturation," Support Portal, Prophesee AI, 2024, access restricted to customers. [Online]. Available: https://support.prophesee.ai/portal/en/kb/articles/sensor-readout-saturation

[44] P. Lichtsteiner, C. Posch, and T. Delbruck, "A 128× 128 120 db 15 μs latency asynchronous temporal contrast vision sensor," *IEEE Journal of Solid-State Circuits*, vol. 43, no. 2, pp. 566–576, 2008.

[45] M. Litzenberger *et al.*, "Embedded vision system for real-time object tracking using an asynchronous transient vision sensor," in *2006 IEEE 12th Digital Signal Processing Workshop 4th IEEE Signal Processing Education Workshop*, 2006, pp. 173–178.

[46] T. Brewer and M. Hawks, "A comparative evaluation of the fast optical pulse response of event-based cameras," in *Image Sensing Technologies: Materials, Devices, Systems, and Applications VIII*, vol. 11723. SPIE, 2021, pp. 86–103.

[47] A. Mitrokhin *et al.*, "Event-based moving object detection and tracking," in *2018 IEEE/RSJ International Conference on Intelligent Robots and Systems (IROS)*, 2018, pp. 1–9.

[48] E. Mueggler, B. Huber, and D. Scaramuzza, "Event-based, 6-dof pose tracking for high-speed maneuvers," in *2014 IEEE/RSJ International Conference on Intelligent Robots and Systems*, 2014, pp. 2761–2768.

[49] E. Mueggler *et al.*, "Continuous-time visual-inertial odometry for event cameras," *IEEE Transactions on Robotics*, vol. 34, no. 6, pp. 1425–1440, 2018.

[50] H. Kim, S. Leutenegger, and A. J. Davison, "Real-time 3d reconstruction and 6-dof tracking with an event camera," in *Computer Vision – ECCV 2016*, B. Leibe *et al.*, Eds. Cham: Springer International Publishing, 2016, pp. 349–364.

[51] H. Rebecq *et al.*, "Emvs: Event-based multi-view stereo—3d reconstruction with an event camera in real-time," *International Journal of Computer Vision*, vol. 126, no. 12, pp. 1394–1414, 2018.

[52] R. Benosman *et al.*, "Event-based visual flow," *IEEE Transactions on Neural Networks and Learning Systems*, vol. 25, no. 2, pp. 407–417, 2014.

[53] A. Z. Zhu *et al.*, "Ev-flownet: Self-supervised optical flow estimation for event-based cameras," *arXiv preprint arXiv:1802.06898*, 2018.

[54] H. Rebecq *et al.*, "High speed and high dynamic range video with an event camera," *IEEE Transactions on Pattern Analysis and Machine Intelligence*, vol. 43, no. 6, pp. 1964–1980, 2021.

[55] C. Scheerlinck *et al.*, "Fast image reconstruction with an event camera," in *Proceedings of the IEEE/CVF Winter Conference on Applications of Computer Vision*, 2020, pp. 156–163. [Online]. Available: https://openaccess.thecvf.com/content_WACV_2020/html/Scheerlinck_Fast_Image_Reconstruction_with_an_Event_Camera_WACV_2020_paper.html

[56] H. Rebecq *et al.*, "Events-to-video: Bringing modern computer vision to event cameras," in *Proceedings of the IEEE/CVF Conference on Computer Vision and Pattern Recognition*, 2019, pp. 3857–3866. [Online]. Available: http://openaccess.thecvf.com/content_CVPR_2019/html/Rebecq_Events-To-Video_Bringing_Modern_Computer_Vision_to_Event_Cameras_CVPR_2019_paper.html

[57] S. Shiba *et al.*, "Event-based background-oriented schlieren," *IEEE Transactions on Pattern Analysis and Machine Intelligence*, vol. 46, no. 4, pp. 2011–2026, 2024.

[58] Z. Lyu, W. Cai, and Y. Liu, "An event-triggered background-oriented schlieren technique combined with dynamic projection using dynamic mirror device," *Measurement Science and Technology*, vol. 35, no. 10, p. 105302, jul 2024.

[59] R. S. Dimitrova *et al.*, "Towards low-latency high-bandwidth control of quadrotors using event cameras," in *2020 IEEE International Conference on Robotics and Automation (ICRA)*, 2020, pp. 4294–4300.

[60] J. Xu *et al.*, "Taming event cameras with bio-inspired architecture and algorithm: a case for drone obstacle avoidance," in *Proceedings of the 29th annual international conference on mobile computing and networking*, 2023, pp. 1–16.

[61] S. Tulyakov *et al.*, "Learning an event sequence embedding for dense event-based deep stereo," in *Proceedings of the IEEE/CVF International Conference on Computer Vision (ICCV)*, October 2019. [Online]. Available: http://openaccess.thecvf.com/content_ICCV_2019/html/Tulyakov_Learning_an_Event_Sequence_Embedding_for_Dense_Event-Based_Deep_Stereo_ICCV_2019_paper.html

[62] C. Willert and J. Klinner, "Event-based imaging velocimetry applied to a cylinder wake flow in air," in *20th International Symposium on Application of Laser and Imaging Techniques to Fluid Mechanics*, 2022.

[63] L. Fan *et al.*, "High-resolution velocimetry technique based on the decaying streaks of phosphor particles," *Opt. Lett.*, vol. 46, no. 3, pp. 641–644, 2021.

[64] B. Fond, C. Abram, and F. Beyrau, "On the characterisation of tracer particles for thermographic particle image velocimetry," *Applied Physics B*, vol. 118, no. 3, pp. 393–399, 2015.

[65] A. I. Maqueda *et al.*, "Event-based vision meets deep learning on steering prediction for self-driving cars," in *Proceedings of the IEEE conference on computer vision and pattern recognition*, 2018, pp. 5419–5427. [Online]. Available: http://openaccess.thecvf.com/content_cvpr_2018/html/Maqueda_Event-Based_Vision_Meets_CVPR_2018_paper.html

[66] D. Gehrig *et al.*, "End-to-end learning of representations for asynchronous event-based data," in *Proceedings of the IEEE/CVF International Conference on Computer Vision*, 2019, pp. 5633–5643. [Online]. Available: http://openaccess.thecvf.com/content_ICCV_2019/html/Gehrig_End-to-End_Learning_of_Representations_for_Asynchronous_Event-Based_Data_ICCV_2019_paper.html

[67] G. Xuan *et al.*, "High spatial resolution fluid thermometry in boundary layers by macroscopic imaging of individual phosphor tracer particles," *Experimental Thermal and Fluid Science*, vol. 148, p. 110977, 2023.

[68] S. Discetti and F. Coletti, "Volumetric velocimetry for fluid flows," *Measurement Science and Technology*, vol. 29, no. 4, p. 042001, 2018.

[69] A. Sciacchitano, B. Wieneke, and F. Scarano, "PIV uncertainty quantification by image matching," *Measurement Science and Technology*, vol. 24, no. 4, p. 045302, 2013.

[70] B. Wieneke, "PIV uncertainty quantification from correlation statistics," *Measurement Science and Technology*, vol. 26, no. 7, p. 074002, 2015.

[71] C. Willert, "Event-based particle image velocimetry for high-speed flows," *Measurement Science and Technology*, vol. 36, no. 7, p. 075302, 2025.